

Article

Two-Stage Locating and Capacity Optimization Model for the Ultra-High-Voltage DC Receiving End Considering Carbon Emission Trading and Renewable Energy Time-Series Output Reconstruction

Lang Zhao ^{1,2}, Zhidong Wang ¹, Hao Sheng ^{2,*}, Yizheng Li ¹, Tianqi Zhang ¹, Yao Wang ³ and Haifeng Yu ⁴

¹ State Grid Economic and Technological Research Institute Co., Ltd., Beijing 102209, China; zhaolang@chinasperi.sgcc.com.cn (L.Z.); wangzhidong@chinasperi.sgcc.com.cn (Z.W.); liyizheng@chinasperi.sgcc.com.cn (Y.L.); zhangtianqi@chinasperi.sgcc.com.cn (T.Z.)

² Key Laboratory of Smart Grid of Ministry of Education, Tianjin University, Tianjin 300072, China

³ Economic and Technological Research Institute of State Grid Shanxi Electric Power Co., Ltd., Taiyuan 030021, China; wangyao@chinasperi.sgcc.com.cn

⁴ Economic and Technological Research Institute of State Grid Hunan Electric Power Co., Ltd., Changsha 030021, China; yuhaifeng@chinasperi.sgcc.com.cn

* Correspondence: hao.sheng@tju.edu.cn; Tel.: +86-18001247807

Abstract: With the load center's continuous expansion and development of the AC power grid's scale and construction, the recipient grid under the multi-feed DC environment is facing severe challenges of DC commutation failure and bipolar blocking due to the high strength of AC-DC coupling and the low level of system inertia, which brings many complexities and uncertainties to economic scheduling. In addition, the large-scale grid integration of wind power, photovoltaic, and other intermittent energy sources makes the ultra-high-voltage (UHV) DC channel operation state randomized. The deterministic scenario-based timing power simulation is no longer suitable for the current complex and changeable grid operation state. In this paper, we first start with the description and analysis of the uncertainty in renewable energy (RE) sources, such as wind and solar, and reconstruct the time-sequence power model by using the stochastic differential equation model. Then, a carbon emission trading cost (CET) model is constructed based on the CET mechanism, and the two-stage locating and capacity optimization model for the UHV DC receiving end is proposed under the constraint of dispatch safety and stability. Among them, the first stage starts with the objective of maximizing the carrying capacity of the UHV DC receiving end grid; the second stage checks its dynamic safety under the basic and fault modes according to the results of the first stage and corrects the drop point and capacity of the UHV DC line with the objective of achieving safe and stable UHV DC operation at the lowest economic investment. In addition, the two-stage model innovatively proposes UHV DC relative inertia constraints, peak adjustment margin constraints, transient voltage support constraints under commutation failure conditions, and frequency support constraints under a DC blocking state. In addition, to address the problem that the probabilistic constraints of the scheduling model are difficult to solve, the discrete step-size transformation and convolution sequence operation methods are proposed to transform the chance-constrained planning into mixed-integer linear planning for solving. Finally, the proposed model is validated with a UHV DC channel in 2023, and the results confirm the feasibility and effectiveness of the model.

Keywords: locating and capacity optimization model; UHV DC receiving end; carbon emission trading; renewable energy time-series output reconstruction



Citation: Zhao, L.; Wang, Z.; Sheng, H.; Li, Y.; Zhang, T.; Wang, Y.; Yu, H. Two-Stage Locating and Capacity Optimization Model for the Ultra-High-Voltage DC Receiving End Considering Carbon Emission Trading and Renewable Energy Time-Series Output Reconstruction. *Energies* **2024**, *17*, 5508. <https://doi.org/10.3390/en17215508>

Academic Editor: Frede Blaabjerg

Received: 24 September 2024

Revised: 31 October 2024

Accepted: 31 October 2024

Published: 4 November 2024



Copyright: © 2024 by the authors. Licensee MDPI, Basel, Switzerland. This article is an open access article distributed under the terms and conditions of the Creative Commons Attribution (CC BY) license (<https://creativecommons.org/licenses/by/4.0/>).

1. Introduction

1.1. Research Background

In the context of the carbon peak and carbon neutrality strategy, the large-scale development and utilization of renewable energy (RE) have become crucial measures for transforming China's energy structure. Through the UHV DC grid, substantial RE can be transmitted to load centers in East and South China. However, with the continuous expansion and development of the load center AC grid, the increased feed into the DC environment at the receiving end, coupled with high AC-DC coupling strength, leads to low system inertia. The UHVDC faces significant challenges such as DC commutation failure and bipolar blocking, which introduce complexity and uncertainty into economic scheduling [1–3].

On the one hand, the large-scale integration of wind, solar, and other RE sources has randomized the operation state of the UHV DC channel. The deterministic scenario-based timing power simulation no longer suits the current complex and dynamic grid operation state. On the other hand, with the escalating issues of global warming and the greenhouse effect, countries have introduced carbon emissions trading into the power market. The carbon emissions trading mechanism has become a core means to achieve low-carbon emission reduction in the UHV DC channel and an important way to balance environmental protection with economic benefits [4–6].

Therefore, accurately describing and analyzing the random power output phenomena of wind and solar energy and integrating the carbon emissions trading mechanism into the locating and capacity optimization of the UHV DC channel present current challenges for the optimal scheduling of the UHV DC channel.

1.2. Literature Survey

The existing research on the uncertainty description of wind and solar power in UHV DC channels is mainly focused on stochastic planning and robust optimization methods [7]. Stochastic planning involves using a finite deterministic scenario to simulate different possibilities of random variables. In a study focusing on time-series output reconstruction of photovoltaic systems [8], Monte Carlo simulation and stochastic planning methods were employed to characterize and reduce scenarios for constructing an economic scheduling model for power sources and loads. However, using a limited number of scenarios may overlook the continuity in photovoltaic output. On the other hand, robust optimization represented uncertainty through 'uncertainty sets' and was effective in simulating worst-case scenarios for optimal decision-making. A two-layer robust interval model was developed in a study on wind power output uncertainty [9], but the results were overly conservative and deviated from reality. Recognizing the limitations of these mathematical methods, the paper adopted a stochastic differential equation model to provide a precise mathematical analysis of the stochastic nature of wind and solar power outputs. Stochastic differential equations were characterized by their simplicity and clear structure, making them more suitable for constructing discrete series prediction models across different time scales [10]. Previous studies have utilized stochastic differential equations to model the stochastic behavior of photovoltaic power generation [11], demonstrating the feasibility of their application in this context despite some roughness in the output reconstruction model.

In a study on low-carbon economic optimization for UHV DC channels [12–14], a low-carbon dispatch model was designed based on the carbon emissions trading mechanism, aiming to achieve the minimum carbon emissions target while ensuring safety and reliability [15]. However, it failed to consider the operational economy of the UHV DC channel and the stochastic nature of RE outputs like wind and solar power. A low-carbon planning and scheduling model was proposed for UHV DC channels with the objective of maximizing comprehensive benefits during the planning period in [16]. Nevertheless, it overlooked the impact of the reserve capacity constraint of the energy storage system on the dispatch model and employed a relatively simple prediction model for the stochastic nature of wind and solar power. The spare capacity of traditional energy units and energy

storage system constraints were considered for the economic dispatch of UHV DC channels, transforming these constraints into probabilistic constraints for the solution in [17]. However, it did not address the impact of the carbon emissions trading mechanism on economic dispatch.

To study voltage and frequency stability constraints during the scheduling process of UHV DC channels, the short-circuit ratio index proposed in [18] only considered the interaction between AC and local DC, making it applicable only to a single-DC feeder scenario. To address this limitation, the multi-infeed Interaction Factor (MIIF) as a quantitative index was proposed in [19,20] to describe the strength of mutual coupling between AC buses in DC system converter stations. However, these studies did not consider the possibility of commutation failures or bipolar blocking faults, nor did they provide indexes for the effective assessment of transient voltage enhancement in UHV DC by busbar reactive power support equipment. The rate of change of frequency (RoCoF) metrics was incorporated in an optimization model to determine the system's inertia demand in [21]. The minimum system inertia demand was proposed based on the RoCoF with frequency nadir constraints and was applied to both microgrid and large grid systems in [22]. In [23], it was clarified that the system inertia distribution had spatio-temporal characteristics. Current research studies are mostly constrained from the perspectives of the maximum frequency deviation rate and maximum frequency deviation without addressing UHV DC relative inertia from the perspective of the AC system inertia of the sending grid. UHV DC relative inertia constraints were set to prevent frequency instability in this paper. In [24], a comprehensive assessment of the aging characteristics of GTL oils compared to conventional MO oils under normal conditions was investigated. The effect of oil aging on dissolved gas generation was investigated. For this purpose, another paper analyzed the dissolved gas generation in four existing old transformers of the same oil type (Diala B) and different ratings at the Egyptian Electricity Transmission Company (EETC) [25]. Their comparison strategies can be applied to this article.

1.3. Research Focus and Organization

This study concentrates on the optimal configuration for the UHV DC receiving end considering carbon emission trading (CET) and RE time-series output reconstruction, addressing some of the limitations in existing research. These limitations include the following:

- (1) Addressing the deficiencies in the stochastic simulation of RE output in UHV DC channels, we use stochastic differential equations to mathematically describe and analyze the stochastic output phenomena of wind and solar energy and reconstruct the corresponding stochastic output models.
- (2) Considering the impact of the CET mechanism on the economic dispatch of UHV DC channels, a three-stage step CET cost model is proposed. This model is incorporated into the system objective function to solve the problem, promoting the sustainable operation of a low-carbon economy for UHV DC channels.
- (3) To address the lack of indicators for effectively assessing transient voltage enhancement in UHV DC by bus reactive power support equipment at converter stations, the effective short-circuit ratio (MOESCR) of the UHV DC line is defined. This parameter characterizes the transient reactive power support capability of the converter station busbar, which is utilized to evaluate transient voltage stability in the event of commutation failure. Furthermore, we impose a constraint on the UHV DC relative inertia by considering the AC system inertia of the sending grid for frequency stability, introducing a UHVDC relative inertia constraint to prevent frequency instability.
- (4) A discrete step-size transformation and convolution sequence operation method is proposed. This method involves discretizing the probability density curve data of wind, solar, and load using discrete step-length transformation, followed by the rapid solution of the equivalent load discrete probability sequence within the constraints through convolution sequence operations.

This article is organized as follows. In Section 2, starting with the description and analysis of the uncertainty in RE sources such as wind and solar energy, the stochastic differential equation model is used to reconstruct the time-series power model and construct a carbon emissions trading cost model based on the carbon emissions trading mechanism. In Section 3, a two-stage positioning and capacity optimization model for the UHV DC receiving end is introduced, with dispatch security and stability constraints taken into account. The first stage aims to maximize the grid's carrying capacity at the UHV DC receiving end. In the second stage, the dynamic safety of the system under both normal and fault conditions is assessed based on the results of the first stage. Adjustments to the drop points and capacity of the UHV DC line are made to ensure safe and stable operation with minimal economic investment. In Section 4, the challenge of solving probabilistic constraints within the model is addressed by proposing discrete step-size transformations and convolutional sequence operations. These methods convert the probabilistic constrained planning into mixed-integer linear programming for resolution. Finally, the proposed model is validated using the UHV DC channel in 2023 in Section 5. Finally, the conclusion and limitation analysis of this article are provided in Section 6.

2. RE Time-Series Output Reconstruction Model Based on a Stochastic Differential Equation

2.1. Wind Power Turbine Time-Series Output Reconstruction Model Based on a Stochastic Differential Equation

If the mathematical expectation ($E(x) = \mu$) of the probability density function $f(x)$ is continuous and finite in variance within its domain of definition (l, u) , the stochastic differential equation can be expressed as follows:

$$dX_t = -\theta(X_t - \mu)dt + \sqrt{v(X_t)}dW_t, t \geq 0 \quad (1)$$

where W_t represents standard Brownian motion. θ represents a non-negative coefficient. $v(X_t)$ represents a non-negative function, which is defined on (l, u) . By transforming (1), the equation can be expressed as follows:

$$v(x) = \frac{2\theta}{f(x)} \int_l^x (\mu - y)f(y)dy, x \in (l, u) \quad (2)$$

where $f(x)$ represents the probability density function of the stochastic process X . It is assumed that the wind speed v_{WT} conforms to a Weibull distribution with scale parameter c and shape parameter k [26]. The wind speed can be simulated using the following stochastic differential equations:

$$f_{WT}(x) = \frac{k}{c} \left(\frac{x}{c}\right)^{k-1} \exp\left[-\left(\frac{x}{c}\right)^k\right] \quad (3)$$

$$\mu = E(X) = c\Gamma\left(\frac{1}{k} + 1\right) \quad (4)$$

where μ represents the mean wind speed. $\Gamma(x)$ and $\Gamma(x, a)$ denote the complete and incomplete gamma functions, respectively. Substituting (3) and (4) into (2), Equation (5) can be expressed as follows:

$$v(x) = \frac{2\theta}{\frac{k}{c} \left(\frac{x}{c}\right)^{k-1} \exp\left[-\left(\frac{x}{c}\right)^k\right]} \left(c\Gamma\left(\frac{1}{k} + 1\right) \left(1 - \exp\left[-\left(\frac{x}{c}\right)^k\right]\right) - c\Gamma\left(\left(\frac{x}{c}\right)^k, \frac{1}{k} + 1\right)\right) \quad (5)$$

In summary, the wind turbine output at time t can be generated by iterative calculation using (6) and (7), where Equation (7) represents the wind turbine output characteristic curve.

$$v_{WT}^t = v_{WT}^{t-1} + dX_t \quad (6)$$

$$P_{WT}^t = \begin{cases} 0 & v_{WT}^t \leq v_{ci} \text{ or } v_{WT}^t > v_{co} \\ \frac{v_{WT}^t - v_{ci}}{v_r - v_{ci}} P_{WT,r} & v_{ci} \leq v_{WT}^t \leq v_r \\ P_{WT,r} & v_r \leq v_{WT}^t \leq v_{co} \end{cases} \quad (7)$$

where v_{WT}^t represents the simulated wind speed of the turbine at moment t . $P_{WT,r}$ represents the active power generated by the wind turbine. $P_{WT,r}$ represents the rated power of the wind turbine. v_r represents the rated wind speed of the wind turbine. v_{ci} and v_{co} represent the cut-in and cut-out wind speeds, respectively. Combined with (3)–(7), the probability density function $f_{WT}(P_{WT})$ of the wind turbine power can be determined.

2.2. Solar Power Time-Series Output Reconstruction Model Based on a Stochastic Differential Equation

The output power P_{PV}^t of a distributed photovoltaic power plant can be calculated as follows [27]:

$$P_{PV}^t = m P_{stc} \frac{I(R_t, k_t, I_{0t})}{I_{stc}} [1 + \alpha_T (T_t - T_{STC})] \quad (8)$$

where P_{stc} represents the rated power labeled on the nameplate of the solar panel. m represents the number of solar panels in the distributed PV power plant. T_t represents the air temperature at moment t . α_T denotes the power temperature coefficient of the PV panels. T_{stc} and I_{stc} represent the standard operating temperature and solar radiation intensity labeled on the nameplate, respectively, and $I(R_t, k_t, I_{0t})$ denotes the total radiation intensity of the solar panel considering the factors of solar irradiation and the clear sky index. R_t represents the irradiation intensity ratio between the tilted surface of the solar panel and the ground plane. I_{0t} represents the solar irradiation outside the atmosphere. k_t represents the clear-sky index, which is highly intermittent and random, and is influenced by cloud cover, weather changes, and other factors.

According to (8), the PV power plant output can be divided into deterministic and stochastic parts. The deterministic parts I_{0t} and R_t are related to the relative position of the sun and the Earth, as well as the angle and position of solar panel installation [23]. For the stochastic part of the clear sky index k_t , this method uses stochastic differential equations to simulate the stochastic output of photovoltaic power generation.

The variable $I(R_t, k_t, I_{0t})$ can be calculated by (9).

$$I(R_t, k_t, I_{0t}) = k_t I_{0t} (1 - p + q k_t) R_t + k_t I_{0t} (p - q k_t) \left(\frac{1 + \cos \beta}{2} \right) + k_t I_{0t} \rho \left(\frac{1 - \cos \beta}{2} \right) \quad (9)$$

where β represents the ground inclination angle. ρ represents the reflectivity of the ground. p and q represent parameters related to the atmosphere. Except for k_t , which is a random variable, the rest of the variables can be determined from geographic and temporal information. Therefore, $I(R_t, k_t, I_{0t})$ can be abbreviated as $I(k_t)$ and organized as a quadratic function of the random variable k_t .

$$\begin{aligned} I(k_t) &= A_1 k_t - A_2 k_t^2 \\ A_1 &= \left[R_t + p \left(\frac{1 + \cos \beta}{2} - R_t \right) + \rho \left(\frac{1 - \cos \beta}{2} \right) \right] I_{0t} \\ A_2 &= q \left(\frac{1 + \cos \beta}{2} - R_t \right) I_{0t} \end{aligned} \quad (10)$$

The probability density function of k_t can be expressed as follows:

$$f_{PV}(k_t) = \frac{C [e^{\lambda k_t} (1 - \gamma k_t) - 1]}{k_{th} \lambda \gamma} \quad (11)$$

where k_{th} represents the maximum value of the clear-sky index k_t , which is determined by the weather type. C , γ , and λ represent constants related to the clear-sky index k_t .

According to (10) and (11), the probability density function of $I(k_t)$, which conforms to a normal distribution, can be found as follows:

$$f_{PV}(I(k_t)) = \frac{C \left(k_{th} - \frac{A_1}{2A_2} - \frac{\sqrt{A_1^2 - 4I(k_t)}}{2A_2} \right)}{k_{th} \sqrt{A_1^2 - 4I(k_t)}} \exp \left[\lambda \left(\frac{A_1}{2A_2} - \frac{\sqrt{A_1^2 - 4I(k_t)}}{2A_2} \right) \right] \quad (12)$$

The stochastic differential equation model can be used to mode the time series of total irradiation on solar PV panels.

$$I(k_t) = I(k_{t-1}) + dX_t \quad (13)$$

Combined with (8) and (12), the probability density function $f_{PV}(P_{PV})$ of the distributed PV plant can be simulated. The normal distribution model [28], which has been widely used, is employed to simulate load fluctuations. Its probability distribution is described as follows:

$$f(P_L) = \frac{1}{\sqrt{2\pi}\sigma_L} \exp \left[-\frac{(P_L - \mu_L)^2}{2\sigma_L^2} \right] \quad (14)$$

where P_L represents the actual active power of the load. μ_L and σ_L represent the mean and standard deviation representing the load fluctuation. To facilitate subsequent calculations, the equivalent load P_{EL} is defined as shown in (15).

$$P_{EL} = P_L - P_{PV} - P_{WT} \quad (15)$$

2.3. Carbon Emission Trading Mechanism and Carbon Emission Cost Modeling

There are two main methods for carbon emission allocations: the historical allocation method and the baseline allocation method [29]. For carbon emissions trading in China based on the benchmark allocation, the benchmark allocation method is used to determine the carbon emission quota. The specific formula is shown in (16).

$$E_q = \theta \sum_{t=1}^T \left(\sum_{m=1}^M P_{MT,mt} + \sum_{n=1}^N P_{PV,nt} + \sum_{w=1}^W P_{WT,nt} \right) \quad (16)$$

where E_q represents the daily carbon emission quota. θ represents the carbon emission benchmark per unit of power generation. T is the dispatch cycle; M , N , and W represent the number of thermal units, photovoltaic power generation units, and wind power generating units, respectively. $P_{MT,mt}$, $P_{PV,nt}$, and $P_{WT,w}$ represent the power generation per unit of thermal generation, photovoltaic power generation, and wind turbine generating units, respectively. Since photovoltaic and wind power are clean energy sources, the main source of carbon emissions is traditional thermal generation. Therefore, the total carbon emission E_p of the active distribution system in the dispatch cycle is described as follows:

$$E_p = \sum_{t=1}^T \sum_{m=1}^M \eta_m P_{MT,mt} \quad (17)$$

where E_p represents the total daily carbon emission. H_m represents the carbon emission per unit of power generated by the m -th traditional thermal units.

To effectively control the disorderly carbon emissions of some enterprises, this method mimics the tariff ladder model and constructs a three-stage stepped carbon emission cost model as follows:

$$f_e = \begin{cases} \lambda(E_p - E_q) & E_p - E_q \leq d \\ (1 + \tau)\lambda(E_p - E_q) - \tau\lambda d & d \leq E_p - E_q \leq 2d \\ (1 + 2\tau)\lambda(E_p - E_q) - 3\tau\lambda d & E_p - E_q > 2d \end{cases} \quad (18)$$

where f_e represents the daily carbon emission cost. λ represents the trading price per unit of carbon emission. τ represents the increase in the carbon emission price at each step; τ represents the interval of the step carbon emission cost. The three-stage stepped carbon emission cost model is shown in Figure 1.

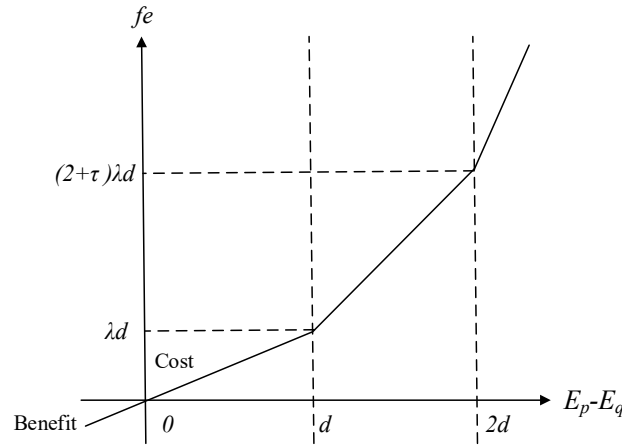


Figure 1. Three-step carbon emission cost model.

3. Two-Stage Locating and Capacity Optimization Model for the UHV DC Receiving End Considering Carbon Emission Trading and RE Time-Series Output Reconstruction

This section proposes a two-stage assessment method of UHV DC construction carrying capacity considering feeder/receiver grid coordination under security and stability constraints. Among them, the first stage starts from the decision-making and assessment of UHV DC line capacity with the objective of maximizing the carrying capacity of the UHV DC feeder–receiver grid. The second stage calibrates its dynamic safety under basic and fault patterns according to the results of the first stage. The relative inertia constraint of UHV DC, the peak adjustment margin constraint, the transient voltage support constraint under the commutation failure condition, and the frequency support constraint under the DC blocking state are innovatively added. Under these safety and stability constraints, the drop point and capacity of UHV DC lines are corrected with the objective of minimizing economic cost and maximizing network utilization efficiency.

3.1. Stage 1: Decision-Making Method for UHV DC Line Capacity with the Objective of Maximizing the Carrying Capacity of the UHV DC Feeder–Receiver Grid

Decision-making and evaluation of the locating and capacity of UHV DC lines are conducted with the objective of maximizing the grid's carrying capacity at the receiving end of the UHV DC feeder. The objective function is represented as follows:

$$\max f_A = \sum_{i \in \Omega_h} Ph_i^R \quad (19)$$

where $\max f_A$ represents the maximum capacity of the receiving end grid that can accommodate the UHV DC feed-in. Ω_h represents the candidate set of pre-installed UHV DC lines. Ph_i^R represents the rated capacity of the i -th UHV DC line.

The primary stage constraints consist of UHV DC line specification constraints, active sufficiency constraints, and UHV DC relative inertia constraints.

(1) UHV DC line specification constraint.

UHV DC lines along the same planning path have varying DC transmission capacities and voltage level specifications due to differing power demands of the receiving grid.

Therefore, planning must be carried out based on different voltage levels and capacity grades. The specification constraints of UHV DC lines are as follows:

$$\begin{aligned} Ph_i^R &= Ph_i^1\alpha_i + Ph_i^2\beta_i + Ph_i^3\gamma_i, \quad \forall i \in \Omega_h \\ \alpha_i + \beta_i + \gamma_i &\leq 1, \quad \forall i \in \Omega_h \end{aligned} \quad (20)$$

where 0–1 integer variables α_i , β_i , and γ_i are utilized to determine the construction specification of the i -th UHV DC line. The current UHV construction levels are ± 1100 kV, ± 800 kV, and ± 500 kV for α_i , β_i , and γ_i , respectively. When $\alpha_i = 1$, $\beta_i = 0$, and $\gamma_i = 0$, it indicates that the i -th UHV DC line is constructed according to the ± 1100 kV specification; when $\alpha_i = 0$, $\beta_i = 1$, and $\gamma_i = 0$, it indicates construction according to the ± 800 kV specification; when $\alpha_i = 0$, $\beta_i = 0$, and $\gamma_i = 1$, it indicates construction according to the ± 500 kV specification; and when $\alpha_i = 0$, $\beta_i = 0$, $\gamma_i = 0$, it means the requirements are not met and the i -th UHV DC line is not constructed. Ph_i^1 , Ph_i^2 , and Ph_i^3 represent the rated capacities of the i -th UHV DC line constructed according to the ± 1100 kV, ± 800 kV, and ± 500 kV standards, which are 6000 MW, 4000 MW, and 2000 MW, respectively.

(2) Active sufficiency constraint.

To ensure that the capacity of UHV DC line construction meets the active transmission requirements of the power source at the sending end and the power grid at the receiving end, the active margin constraint is set as follows:

$$\begin{aligned} \sum_{i \in \Omega_h} Ph_i^R &\geq (1 + GI) \left(\sum_{j \in \Omega_w} Pw_j^{\max} + \sum_{k \in \Omega_z} Pz_k^{\max} + \sum_{m \in \Omega_g} Pg_m^{\max} \right), \quad \forall i \in \Omega_h, j \in \Omega_w, k \in \Omega_z, m \in \Omega_g \\ \sum_{i \in \Omega_h} Ph_i^R &\geq (1 + RI) Pl^{\max}, \quad \forall i \in \Omega_h \end{aligned} \quad (21)$$

where Pw_j^{\max} , Pz_k^{\max} , and Pg_m^{\max} represent the maximum technical output of wind turbine j , photovoltaic power station k , and thermal power unit m , respectively. Ω_w , Ω_z , and Ω_g represent the collection of wind turbines, photovoltaic power stations, and thermal power units of large-scale energy bases, respectively. Pl^{\max} is the maximum load of the receiving-end grid. GI and RI represent the generating and load sufficiency coefficients, set to be 0.3.

(3) UHV DC relative inertia constraints.

As the proportion of UHV DC power supply increases, the rotational inertia of the AC system must meet high requirements to ensure system frequency stability. However, unlike traditional thermal power units, the output power of new energy units is solely dependent on natural factors (wind speed, light intensity), and their grid-connected power electronic components such as converters decouple active power and frequency changes, lacking the moment of inertia. This absence of rotational inertia in the AC system also limits UHVDC transmission capacity. The UHV DC relative inertia constraint is represented as follows:

$$\begin{aligned} H_{UHV} &= \frac{J_{AC}}{\sum_{i \in \Omega_h} Ph_i^R} = \frac{\sum_{m \in \Omega_g} H_m P_{g_m}^{\max}}{\sum_{i \in \Omega_h} Ph_i^R} \\ H_{UHV} &\geq H_{DC}^{\min} \end{aligned} \quad (22)$$

where H_g denotes the inertia time constant of thermal power unit m , set to 2.8. J_{AC} represents the total inertia of the AC system. H_{UHV} denotes the equivalent inertia time constant of the UHV DC. H_{DC}^{\min} signifies the minimum equivalent inertia time constant satisfied by the UHV DC, set to 3.

3.2. Stage 2: Installation Location and Capacity Modification Model Aiming to Minimize Investment Costs and Maximize Network Operating Efficiency

The second stage involves the calibration of a safe operation model, which optimizes system investment and operational economics by efficiently managing the output of each type of unit and the allocation of system rotational reserves. It also verifies the feasibility of the decision schemes from the first stage by evaluating all potential fault scenarios. Thus, the second stage aims to minimize investment and operating costs while maximizing grid operating efficiency. The investment and operating costs include standby costs, load-shedding penalty costs, construction costs, and operation and maintenance costs.

$$\min f_{B1} = \sum_{s \in \Omega_s} \sum_{t \in \Omega_t} \sum_{i \in \Omega_h} r_i (Rh_{s,t,i}^{up} + Rh_{s,t,i}^{down}) + \sum_{s \in \Omega_s} \sum_{t \in \Omega_t} \sum_{d \in \Omega_d} d_t Pd_{s,t,d} + \sum_{i \in \Omega_h} l_i p_i (C_{v,i} + C_{m,i}) \quad (23)$$

where Ω_h represents the candidate set of pre-commissioned i -th UHV DC line. Ω_s denotes the set of operational scenarios s (including normal and faulty operation scenarios). Ω_t represents the set of operational moments t . Ω_d represents the set of operational DC faults d . r_i represents the unit standby cost coefficient of UHV DC line i (set at CNY 320/MW). $Rh_{s,t,i}^{up}$ and $Rh_{s,t,i}^{down}$ denote the upper and lower standby capacities of UHV DC line i at moment t . d_t represents the load-shedding penalty factor at moment t (set at CNY 2000/MW). $Pd_{s,t,d}$ represents the amount of load-shedding in the event of a DC fault d at moment t . l_i and p_i denote the length of the construction of the i -th UHV DC line and the construction specification factor (set at 1.2 for ± 1100 kV, 1.0 for ± 800 kV, and 0.8 for ± 500 kV). $C_{v,i}$ and $C_{m,i}$ represent the construction cost and maintenance cost per unit length (set at CNY 260 million, CNY 170 million, and CNY 120 million versus CNY 0.15 million, CNY 0.13 million, and CNY 0.11 million per kilometer for the three voltage levels, respectively).

The operation efficiency of the UHV DC line is expressed as the amount of electricity from wind turbines, photovoltaic power plants, and thermal power units delivered to the UHV line under various scenarios, divided by the amount of electricity transmitted according to the rated capacity of the UHV line. Therefore, the maximum objective function of grid operation efficiency is shown as follows:

$$\max f_{B2} = \frac{\sum_{s \in \Omega_s} \sum_{t \in \Omega_t} \left(\sum_{j \in \Omega_w} Pw_{s,t,j} + \sum_{k \in \Omega_z} Pz_{s,t,k} + \sum_{m \in \Omega_g} Pg_{s,t,m} \right)}{ST \sum_{i \in \Omega_h} Ph_i^R} \quad (24)$$

where S and T represent the total number of operating scenarios s and operating moments t , respectively; $Pw_{s,t,j}$, $Pz_{s,t,k}$, and $Pg_{s,t,m}$ denote the outputs of wind turbine j , photovoltaic power plant k , and thermal power generator m in scenario s at moment t .

Since the two optimization objectives in the second stage have different magnitudes, this study sets the deviation satisfaction function to find the global optimal solution with the objective of minimizing the deviation satisfaction.

$$\min \psi = \delta_1 \left| \frac{f_{B1} - f_{B1}^*}{f_{B1}^*} \right| + \delta_2 \left| \frac{f_{B2} - f_{B2}^*}{f_{B2}^*} \right| \quad (25)$$

where δ_1 and δ_2 represent the deviation satisfaction weight values, and f_{B1}^* and f_{B2}^* represent the optimal values of the objective function under single objective, respectively.

The second stage constraints include the unit output constraints at steady state, the UHV DC operation constraints, the peaking margin constraints, the transient voltage support constraints under commutation failure conditions, and the frequency support constraints under DC blocking conditions during a fault.

(1) Unit output constraint.

$$\begin{aligned} Pw_j^{\min} &\leq Pw_{s,t,j} \leq Pw_j^{\max} \\ Pz_k^{\min} &\leq Pz_{s,t,k} \leq Pz_k^{\max} \\ Pg_m^{\min} &\leq Pg_{s,t,m} \leq Pg_m^{\max} \end{aligned} \quad (26)$$

where Pw_j^{\min} , Pz_k^{\min} , and Pg_m^{\min} represent the minimum technical outputs of wind turbine j , photovoltaic power plant k , and thermal power unit m , respectively.

(2) UHV DC operation constraint.

Restricted by converter polarity changes and conductor thermal stability limits, the UHV DC current direction cannot be changed frequently, and its adjustment times are constrained. Additionally, UHV DC is subject to operating power magnitude constraints, power creep constraints, and adjustment constraints during steady-state operation.

$$Ph_i^{\min} \leq Ph_{s,t,i} \leq Ph_i^R \quad (27)$$

Equation (27) represents the UHV DC operation power magnitude constraint, where $Ph_{s,t,i}$ denotes the transmission power of UHV DC line i at moment t in scenario s , and Ph_i^{\min} denotes the minimum transmission power of UHV DC line i (5000 MW, 2000 MW, and 1000 MW, respectively, according to voltage level).

$$Rh_i^{\text{down}} I_{s,t,i}^{\text{down}} \leq Ph_{s,t,i} - Ph_{s,t-1,i} \leq Rh_i^{\text{up}} I_{s,t,i}^{\text{up}} \quad (28)$$

Equation (28) represents the UHV DC operation power glide and climb constraints, Rh_i^{up} and Rh_i^{down} denote the maximum glide and climb power specified for UHV DC line i (set to 300 and 200 MW/min), and $I_{s,t,i}^{\text{up}}$ and $I_{s,t,i}^{\text{down}}$ denote 0–1 variables indicating whether the upward and downward power of the UHV DC line i at moment t in scenario s is adjusted (0 means no action, 1 means action).

$$I_{s,t,i}^{\text{down}} + I_{s,t,i}^{\text{up}} = U_{s,t,i} \leq 1 \quad (29)$$

$$\begin{aligned} I_{s,t,i}^{\text{down}} + I_{s,t-1,i}^{\text{up}} &\leq 1 \\ I_{s,t-1,i}^{\text{down}} + I_{s,t,i}^{\text{up}} &\leq 1 \end{aligned} \quad (30)$$

Equation (29) indicates that only upward or downward power adjustment can be performed at the same moment, and $U_{s,t,i}$ represents a 0–1 variable indicating whether or not the adjustment is performed for moment t in scenario s for UHV DC line i . Equation (30) indicates that no opposite power adjustment can be performed at adjacent moments.

$$\sum_{t=T_{i,\min}+1} (1 - U_{s,t,i}) \geq T_{i,\min} (U_{s,t,i} - U_{s,t-1,i}) \quad (31)$$

$$\sum_{t \in \Omega_T} (I_{s,t,i}^{\text{down}} + I_{s,t,i}^{\text{up}}) \leq N_h \quad (32)$$

Equation (31) represents the maximum time limit for the constant power operation of UHV DC line i . $T_{i,\min}$ represents the minimum time for the constant power operation of UHV DC line i (set to 1 h). Equation (32) represents the intra-day tidal current number adjustment limit. N_h represents the maximum number of intra-day tidal current number adjustments (10 times/day).

(3) Peak margin constraint.

The peak-to-valley difference in the load of the power grid at the receiving end increases because the thermal power units at the generating end and the extra-high-voltage lines at the transmission end are responsible for the standby demand. It is necessary to ensure that the generating power and the transmission power meet the peak shifting

margin requirements. This study uses high and low peak capacity margins (PCP, TCP) to characterize the peaking margin constraints.

$$\frac{\sum_{m \in \Omega_g} P g_m^{\max}}{\max_{s \in \Omega_s, t \in \Omega_T} \left\{ P l_{s,t} - \sum_{m \in \Omega_g} P g_{s,t,m} \right\} + \sum_{s \in \Omega_s, t \in \Omega_t, m \in \Omega_g} R g_{s,t,m}^{up}} \geq PCP_{\min} \tag{33}$$

$$\frac{\sum_{i \in \Omega_h} P h_i^{\max}}{\max_{s \in \Omega_s, t \in \Omega_T} \left\{ P l_{s,t} - \sum_{i \in \Omega_h} P h_{s,t,i} \right\} + \sum_{s \in \Omega_s, t \in \Omega_t, i \in \Omega_h} R h_{s,t,i}^{up}} \geq PCP_{\min}$$

$$\frac{\sum_{m \in \Omega_g} P g_m^{\min}}{\min_{s \in \Omega_s, t \in \Omega_T} \left\{ P l_{s,t} - \sum_{m \in \Omega_g} P g_{s,t,m} \right\} - \sum_{s \in \Omega_s, t \in \Omega_t, m \in \Omega_g} R g_{s,t,m}^{down}} \geq TCP_{\min} \tag{34}$$

$$\frac{\sum_{i \in \Omega_h} P h_i^{\min}}{\min_{s \in \Omega_s, t \in \Omega_T} \left\{ P l_{s,t} - \sum_{i \in \Omega_h} P h_{s,t,i} \right\} - \sum_{s \in \Omega_s, t \in \Omega_t, i \in \Omega_h} R h_{s,t,i}^{down}} \geq TCP_{\min}$$

Equations (33) and (34) represent the minimum peaking margins required for thermal power units at the generation end and UHV lines at the transmission end during peak and trough times, respectively. $P l_{s,t}$ represents the load on the receiving end of the grid at moment t in scenario s . $P g_{s,t,m}^{up}$ and $P g_{s,t,m}^d$ represent the maximum glide and creeping power rate of the thermal power units m at moment t (set to 100 and 50 MW/min). PCP^{min} and TCP^{min} represent the minimum high and low peak capacity margins required for safe and stable operation (set to 1.8 and 1.5).

(4) Transient voltage support constraints under commutation failure conditions.

When addressing faults that cause DC commutation failure, the converter station bus is equipped with reactive power support equipment, such as regulators, to ensure the rapid recovery of UHV DC voltage. Thus, it is necessary to constrain the capacity of reactive power support. In this paper, the effective short-circuit ratio (MOESCR) of the UHV DC line is defined to characterize the transient reactive power support capacity of the converter station bus.

$$MOESCR_i = \frac{-Q_i + \sum_q \eta_{iq} Q_{iq}}{P h_i^R + \sum_q \frac{Z_{iq}}{Z_{qq}} P_{iq}} \tag{35}$$

$$MOESCR_i \geq MOESCR_{\min}$$

where $MOESCR_i$ represents the effective short-circuit ratio of the i -th UHV DC line. $MOESCR_{\min}$ represents the threshold value of the effective short-circuit ratio of the UHV DC line, set to 2.6. Q_i represents the reactive power required to restore voltage under the commutation failure condition of the i -th UHV DC line; η_{iq} is a 0–1 variable indicating whether the reactive power support equipment at node q has an effect on voltage restoration for DC line i (0 means no, 1 means yes). Q_{iq} represents the reactive power provided by the reactive support equipment at node q to DC line i . P_{iq} represents the active power flowing into DC line i from node q . Z_{iq} represents the impedance from node q to DC line i . Z_{qq} represents the self-impedance of node q .

(5) Transient voltage stability constraints.

The constraints for high and low voltage ride-through requirements stipulate the restoration of transient voltage to specific percentages of the original bus voltage after a fault. For instance, 1 s, 10 s, and 60 s after a fault during low-voltage ride-through require the voltage to be restored to 75%, 80%, and 90% of the original bus voltage, while 0.5 s, 1 s, and 10 s after a fault during high-voltage ride-through specify that the voltage cannot exceed 130%, 125%, and 120%.

$$\begin{aligned} U_{i(t_0+1)} &\geq 0.75U_{is0} & U_{i(t_0+0.5)} &\leq 1.3U_{is0} \\ U_{i(t_0+10)} &\geq 0.8U_{is0} & U_{i(t_0+1)} &\leq 1.25U_{is0} \\ U_{i(t_0+60)} &\geq 0.9U_{is0} & U_{i(t_0+10)} &\leq 1.2U_{is0} \end{aligned} \quad (36)$$

where $U_{i(t_0+x)}$ represents the node i voltage after x seconds of the fault. U_{is0} represents the steady-state voltage of node i before the fault.

(6) Frequency support constraint under dc blocking conditions.

When the commutation failure condition deteriorates further, it can lead to bipolar blocking in the UHV DC line. Load-shedding measures are then allowed to ensure grid frequency and current stability. Consequently, the following constraints need to be added to the safety calibration model:

$$\begin{aligned} 0 &\leq \Delta Pd_{s,t,i}^k \leq \mu_i Pd_{s,t,i} \\ \Delta Pd_{s,t,i}^k &\leq \Delta Pd^{\max} \end{aligned} \quad (37)$$

where $\Delta Pd_{s,t,i}^k$ represents the load-shedding amount for DC blocking fault k at moment t in scenario s . μ_i represents the load-shedding coefficient of the i -th UHV DC line, set to 0.3, and ΔPd^{\max} represents the maximum permissible load-shedding amount, set to 500 MW.

$$\Delta P_{s,t}^k - \sum_{i \in \Omega_{ds}} \Delta Pd_{s,t,i}^k \leq \sum_{i \in \Omega_h} Rh_{s,t,i}^{up} \quad (38)$$

Equation (38) represents the unbalanced power after the primary frequency modulation standby is greater than the load-shedding action. Ω_{ds} represents the set of nodes with automatic load-shedding devices. $\Delta P_{s,t}^k$ represents the unbalanced power generated by DC blocking faults at moment t in scenario s .

$$\frac{\Delta P_{s,t}^k - \sum_{i \in \Omega_{ds}} \Delta Pd_{s,t,i}^k}{2J_{AC}/f_0} \leq RoCoF_{\max} \quad (39)$$

Equation (39) represents the system frequency change without exceeding the limits under the remaining unbalanced power after load-shedding. $RoCoF_{\max}$ represents the maximum rate of change in frequency of the system. f_0 represents the rated frequency (50 Hz).

$$\frac{\Delta P_{s,t}^k - \sum_{i \in \Omega_{ds}} \Delta Pd_{s,t,i}^k - \sum_{i \in \Omega_h} Rh_{s,t,i}^{up}}{\left| D\left(\sum_{s \in \Omega_s} \sum_{t \in \Omega_t} \sum_{d \in \Omega_d} Pd_{s,t,d} - \sum_{i \in \Omega_{ds}} \Delta Pd_{s,t,i}^k \right) \right|} \leq \Delta f_{\max} \quad (40)$$

Equation (40) indicates that after load-shedding, the system frequency change does not exceed the maximum deviation and does not cause instability. Δf_{\max} represents the maximum frequency deviation of the system. $D()$ represents the load sag primary function (load variation versus frequency variation curve $\Delta f = -0.002Pd + 0.0035$).

(7) Reserve capacity probability constraints.

In the UHV DC transmission system, a certain amount of reserve capacity is required to compensate for discrepancies between the actual and predicted power levels, ensuring the safe and reliable operation of the system.

$$\begin{aligned} R_{MTm,t} &\leq U_{m,t} P_{MTm}^{\max} - P_{MTm,t} \\ R_{ESS,t} &\leq \min(\eta_{dch} \frac{SOC_t - SOC_{\min}}{\Delta t} P_{dch}^{\max} - P_{dch,t}) \end{aligned} \tag{41}$$

where $R_{MTm,t}$ and $R_{ESS,t}$ represent the standby capacity of the thermal power unit and energy storage system at time t , respectively. The standby capacity is represented by probabilistic constraints as follows:

$$f_P \left\{ \begin{aligned} &\sum_{m=1}^M R_{MTm,t} + R_{ESS,t} \geq \\ &P_{L,t} - P_{PV,t} - P_{WT,t} - E(P_{EL,t}) \end{aligned} \right\} \geq \varepsilon \tag{42}$$

where ε represents the confidence level constant for this probabilistic constraint form. $P_{EL,t}$ represents the equivalent load at time t .

4. Two-Stage Locating and Capacity Optimization Model Solving Process and Steps

4.1. Probability Density Series Solution for Equivalent Loads

To calculate the probability density of the equivalent load in Equation (42), let $x = P_L - P_{PV} - P_{WT}$ and $y = P_{PV} + P_{WT}$. The probability density function $f(x)$ of the equivalent load can be expressed as follows:

$$\begin{aligned} f_X(x) &= \int_0^{P_{PV\max}} f_{PV}(P_{PV}) f_{WT}(x - P_{PV}) dP_{PV} \\ F_Y(y) &= \int_{-\infty}^y \left[\int_0^{P_{L\max}} f_X(P_L - y) f_L(P_L) dP_L \right] dy \\ f_Y(y) &= F_Y^{-1}(y) \end{aligned} \tag{43}$$

where, $f_{PV}()$, $f_{WT}()$, and $f_L()$ represent the probability density functions of PV, wind, and load, respectively. From Equation (43), it is evident that the complexity of the probability density function makes its inverse transform processing troublesome. In this paper, we choose discrete step-size transformation, effectively avoiding the inverse function calculation through additive or subtractive convolution operations. Assuming that the wind power output $P_{WT,t}$, photovoltaic power output $P_{PV,t}$, and load $P_{L,t}$ are independent random variables with period t , their continuous probability distributions can be discretized to obtain the corresponding probability sequences $p(i_{p,t})$, $w(i_{w,t})$, and $l(i_{l,t})$. For example, the continuous probability density function of the photovoltaic power output $P_{PV,t}$ is converted into a probability density sequence as shown in (44).

$$p(i_{p,t}) = \begin{cases} \int_0^{q/2} f(P_{PV}) dP_{PV} & i_{p,t} = 0 \\ \int_{i_{p,t}q - q/2}^{i_{p,t}q + q/2} f(P_{PV}) dP_{PV} & i_{p,t} > 0, i_{p,t} \neq N_{p,t} \\ \int_{i_{p,t}q - q/2}^{i_{p,t}q} f(P_{PV}) dP_{PV} & i_{p,t} = N_{p,t} \end{cases} \tag{44}$$

where, q represents the discrete step size. The probability density sequences of wind power output $P_{WT,t}$ and load $P_{L,t}$ can be obtained using the same method. The lengths of the probability sequences $N_{p,t}$, $N_{w,t}$, and $N_{l,t}$ can be determined by (45).

$$\begin{cases} N_{p,t} = P_{PVmax,t}/q \\ N_{w,t} = P_{WTmax,t}/q \\ N_{l,t} = P_{Lmax,t}/q \end{cases} \quad (45)$$

where $P_{PVmax,t}$, $P_{WTmax,t}$, and $P_{Lmax,t}$ represent the maximum output powers of PV, wind, and load at time t . The probability sequence $c(i_{c,t})$ of the PV–wind power combination output and the probability density sequence $e(i_{e,t})$ of the equivalent load can then be expressed by additive or subtractive convolution operations as follows:

$$\begin{aligned} c(i_{c,t}) &= \sum_{i_{p,t}+i_{w,t}=i_{c,t}} p(i_{p,t})w(i_{w,t}) \quad i_{c,t} = 0, 1, \dots, N_{c,t} \\ e(i_{e,t}) &= \begin{cases} \sum_{i_{l,t}-i_{c,t}=i_{e,t}} l(i_{l,t})c(i_{c,t}) & 1 \leq i_{e,t} \leq N_{e,t} \\ \sum_{i_{l,t} \leq i_{c,t}} l(i_{l,t})c(i_{c,t}) & i_{e,t} = 0 \end{cases} \quad (46) \\ N_{c,t} &= N_{p,t} + N_{w,t} \\ N_{e,t} &= N_{l,t} - N_{p,t} + N_{w,t} \end{aligned}$$

For the equivalent load P_{EL} at any moment, there exists a corresponding probability $e(i_e)$. All possible probabilities of occurrence form a probability density sequence $e(i_{e,t})$.

4.2. Transformation Methods for Probabilistic Constraints

To convert Equation (42) from a probabilistic constraint to a deterministic constraint, it is necessary to introduce a new binary variable $\psi_{ie,t}$ in addition to Equation (46), defined as follows:

$$\begin{aligned} \psi_{ie,t} &= \begin{cases} 1 & \sum_{m=1}^M R_{MTm,t} + R_{ESS,t} \geq i_{e,t}q - E(P_{EL,t}) \\ 0 & \sum_{m=1}^M R_{MTm,t} + R_{ESS,t} < i_{e,t}q - E(P_{EL,t}) \end{cases} \quad (47) \\ i_{e,t} &= 0, 1, \dots, N_{e,t} \end{aligned}$$

where $i_{e,t}q$ represents a stepwise representation of $P_{EL,t}$. Thus, $\psi_{ie,t}$ equals 1 when the standby capacity of the UHV DC channel is greater than or equal to the difference between $i_{e,t}q$ and $E(P_{EL,t})$; otherwise, $\psi_{ie,t}$ equals 0. Consequently, Equation (42) can be simplified as follows:

$$\sum_{i_{e,t}=0}^{N_{e,t}} \psi_{ie,t} e(i_{e,t}) \geq \varepsilon \quad (48)$$

To convert Equation (47) into a mixed-integer linear programming problem for solution, additional processing is required, as shown in Equation (49).

$$\begin{aligned} & \frac{\left[\sum_{m=1}^M R_{MTm,t} + R_{ESS,t} - i_{e,t}q + E(P_{EL,t}) \right]}{\lambda} \leq \psi_{ie,t} \\ & \leq 1 + \frac{\left[\sum_{m=1}^M R_{MTm,t} + R_{ESS,t} - i_{e,t}q + E(P_{EL,t}) \right]}{\lambda} \quad (49) \\ & \zeta \leq \psi_{ie,t} \leq 1 + \zeta \\ & -\zeta \leq \psi_{ie,t} \leq 1 - \zeta \end{aligned}$$

where λ is a large positive number and ζ is a small positive number. When the standby capacity exceeds the predicted power error, $\psi_{ie,t}$ can only be 1 (Equation (49)); when the standby capacity is less than the predicted power error, $\psi_{ie,t}$ can only be 0 (Equation (49)). Through the aforementioned method (47)–(49), the probabilistic constrained model can be transformed into a mixed-integer linear programming model.

4.3. Solving Steps of the Two-Stage Locating and Capacity Optimization Model

The flow of the two-stage locating and capacity optimization model for the UHV DC receiving end considering CET and RE time-series output reconstruction is shown in Figure 2 and described below. The Matlab 2021a particle swarm optimization algorithm was utilized to determine the optimal configuration of the locating and capacity for UHV DC.

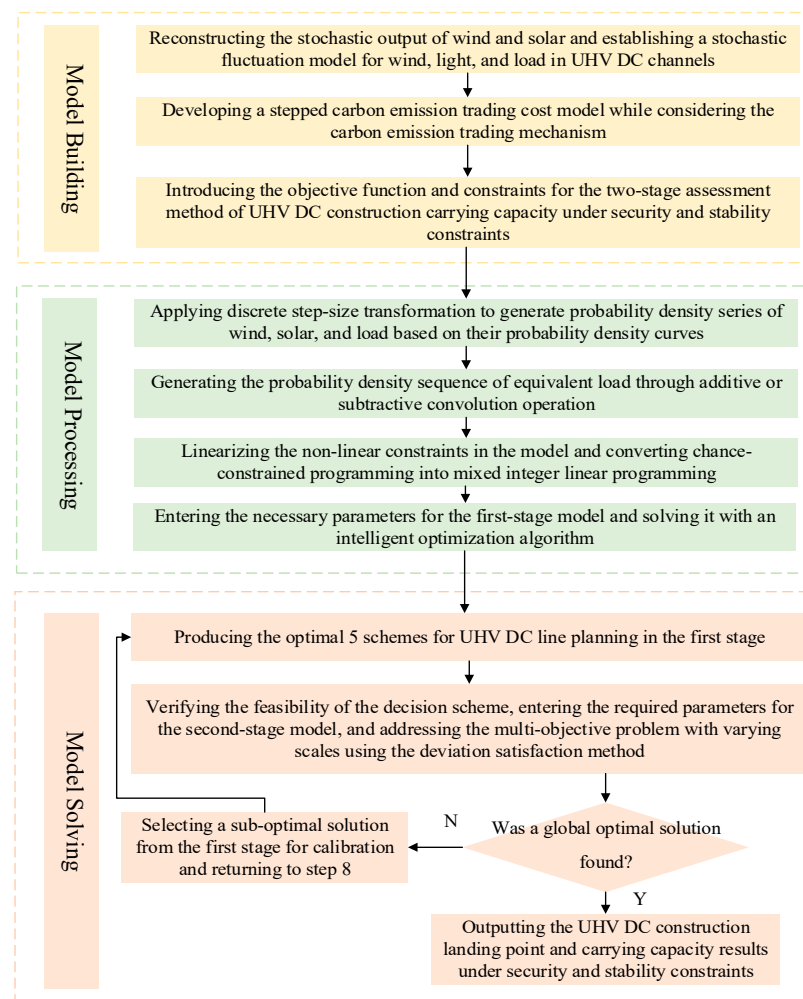


Figure 2. Solving process for the two-stage optimal model.

- (1) Reconstructing the stochastic output of wind and solar and establishing a stochastic fluctuation model for wind, light, and load in UHV DC channels.
- (2) Developing a stepped CET cost model while considering the CET mechanism.
- (3) Introducing the objective function and constraints for the two-stage assessment method of UHV DC construction carrying capacity under security and stability constraints.
- (4) Applying discrete step-size transformation to generate probability density series of wind, solar, and load based on their probability density curves.
- (5) Generating the probability density sequence of equivalent load through additive or subtractive convolution operation.

- (6) Linearizing the non-linear constraints in the model and converting chance-constrained programming into mixed integer linear programming.
- (7) Entering the necessary parameters for the first-stage model and solving it with an intelligent optimization algorithm.
- (8) Producing the optimal scheme for UHV DC line planning in the first stage.
- (9) Entering the required parameters for the second-stage model and addressing the multi-objective problem with varying scales using the deviation satisfaction method.
- (10) Verifying the feasibility of the decision scheme from the first stage in step 8.
- (11) Entering the necessary parameters for the second-stage model and solving it using an intelligent optimization algorithm.
- (12) Proceeding to step 14 if a global optimal solution is found, or else return to step 13.
- (13) Selecting a sub-optimal solution from the first stage for calibration and returning to step 8.
- (14) Outputting the UHV DC construction landing point and carrying capacity results under security and stability constraints.

5. Case Study

5.1. Data Collection and Parameter Selection

The 68-node grid at the sending end of a large energy generation base is the focus of this study, comprising eight large-scale RE farms (total installed capacity of 4080 MW), 10 conventional energy power plants (total installed capacity of 6240 MW), and a set of UHV DC transmission lines (total outgoing power of 5500 MW). The network topology is illustrated in Figure 3. The 500 kV grid framework of a specific province is utilized as the receiving end for analyzing and validating the methodology proposed in this paper, as depicted in Figure 4. Consequently, the DC transmission lines to be constructed are categorized into ‘ ± 800 kV’ and ‘ ± 500 kV’ types based on the voltage level, while the parameters for the proposed model are shown in Table 1.

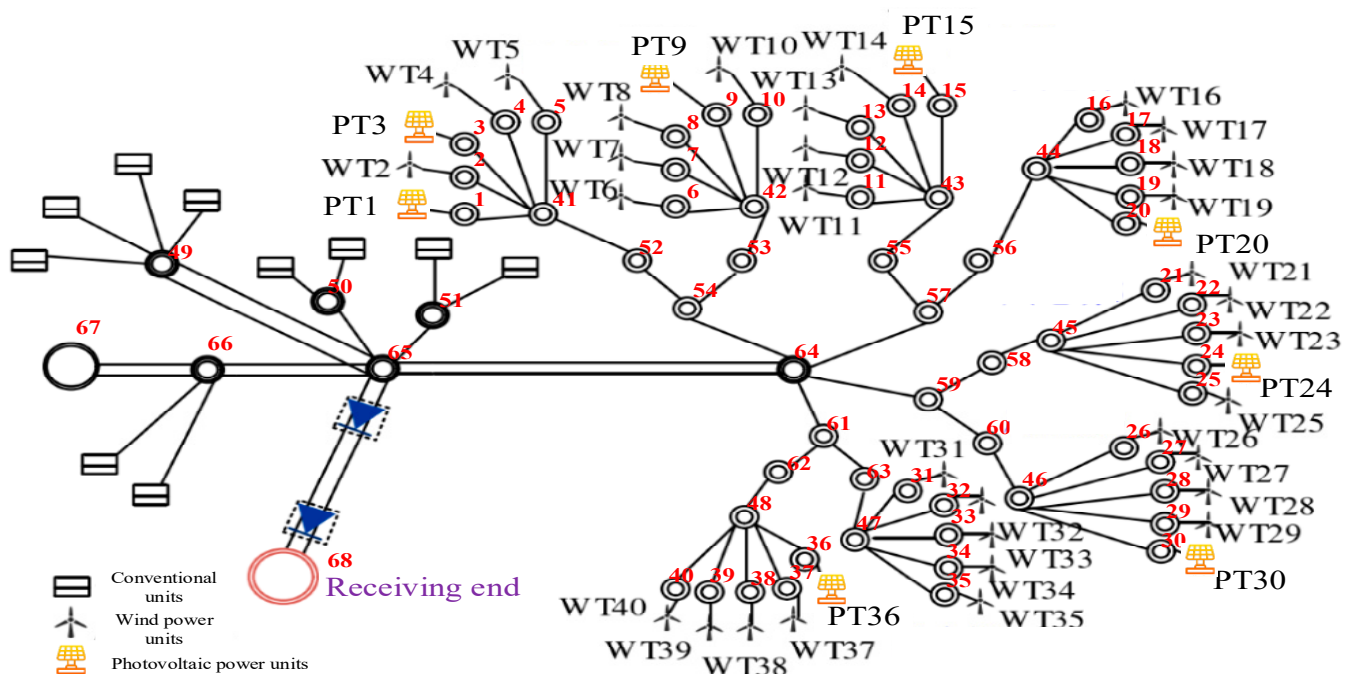


Figure 3. Wiring diagram of the sending-end grid of large energy bases in China.

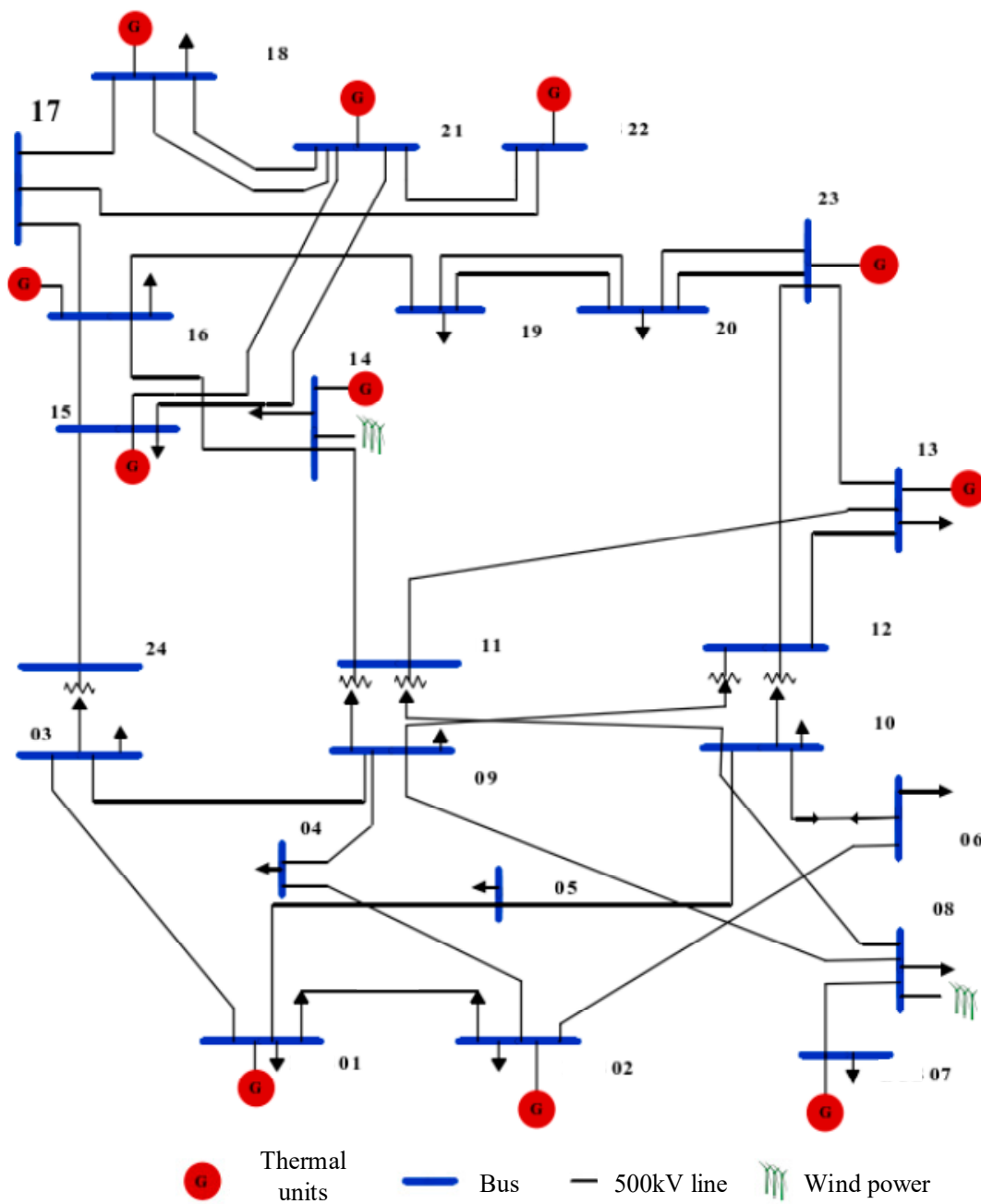


Figure 4. The 500 kV grid framework in China.

Table 1. The parameters for the proposed model.

Parameter	Value	Parameter	Value
The maximum allowable frequency change rate	0.7 Hz/s	The length of the carbon emission interval	40t
The maximum frequency deviation	0.1 Hz	The increase in the carbon emission price	25%
The total inertia of the AC system	16.5	The maximum technical outputs of RE units	6000 MW
The standard deviation of the load	10%	The minimum technical outputs of RE units	1000 MW
The confidence level	0.9	The maximum technical outputs of thermal power units	4200 MW
The carbon trading price	CNY 90/t	The minimum technical outputs of thermal power units	2500 MW

5.2. Two-Stage Locating and Capacity Optimization Results for UHV DC Considering Co-Ordination of the Sending with the Receiving Grid

5.2.1. Stage 1: Decision-Making Results for UHV DC Line Capacity with the Objective of Maximizing the Carrying Capacity of the UHV DC Feeder–Receiver Grid

The effectiveness of the stochastic differential equation-based model for reconstructing RE time-series output was validated using data obtained from a UHV DC channel in 2023. It was compared with the traditional stochastic planning method based on deterministic scenarios, as detailed in Table 2.

Table 2. Comparison of results from stochastic prediction models for RE.

RE Type and Output (MW)		Measured Wind and Photovoltaic Output (MW)	Stochastic Simulation Based on Deterministic Scenarios (MW)	Error from Actual (%)	Time-Series Simulation Based on Stochastic Differential Equations (MW)	Error from Actual (%)
Wind Power Generation	Average Output	1294	1341	3.68	1269	2.32
	Maximum Output	2138	2231	5.69	2068	2.25
Photovoltaic Power Generation	Average Output	1320	1410	6.84	1351	3.63
	Maximum Output	3386	3490	3.22	3445	2.19

The results demonstrate that the time-series simulation method presented in this study effectively reduces the prediction error of wind power and photovoltaic output compared with the traditional method, with a reduction in prediction error of approximately 2% and a significant enhancement in scheduling decision accuracy. It can be seen that the improvement in wind and light prediction accuracy can more accurately judge the transmission capacity of UHV lines, more accurately plan the DC drop point, and improve the efficiency of grid operation. In addition, it can also reduce the cost of load-shedding penalties, improve carbon trading revenue, and increase operating profits. Furthermore, an analysis of the optimal results was conducted by integrating typical daily meteorological data and system parameters of the transmission grid in 2023. The time-series output reconstruction simulation of the UHV DC channel system was performed, showcasing the UHV DC, wind power, and photovoltaic power prediction time-series output curves and discrete sequences, as depicted in Figure 5.

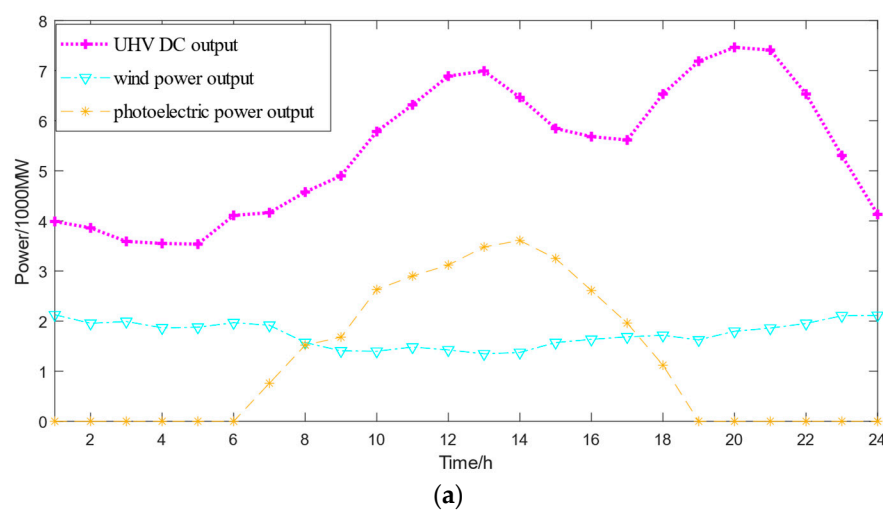


Figure 5. Cont.

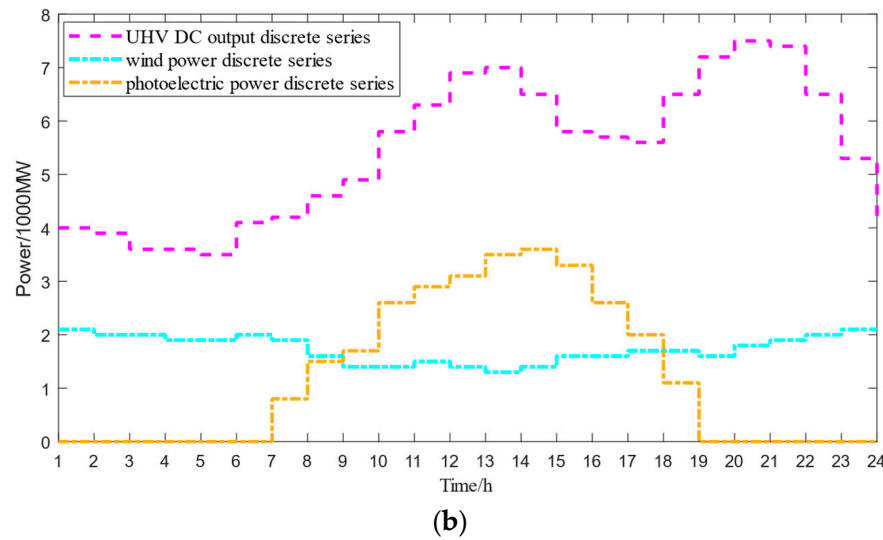


Figure 5. UHV DC, wind power, photoelectric forecast output curve, and discrete series. (a) UHV DC, wind power, and photoelectric forecast output curve. (b) UHV DC, wind power, and photoelectric discrete series after discretization.

According to the UHV DC transmission power in Figure 5, the two-stage UHV DC construction carrying capacity model proposed in this paper was analyzed by example, and the optimization results of stage 1 are shown in Table 3.

Table 3. The optimization results of the typical day stage 1 and stage 2 comparison.

Evaluation Indicators		Comparison of Capacity Results for UHV DC Construction				
		Optimal Scheme 1 of Stage 1	Optimal Scheme 2 of Stage 1	Optimal Scheme 3 of Stage 1	Optimal Scheme 4 of Stage 1	Optimal Scheme 5 of Stage 1
±500 kV	Quantity	2	2	2	1	3
	Drop point	9, 17	17, 23	3, 17	15, 17, 23	9, 15, 17
±800 kV	Quantity	2	2	2	3	1
	Drop point	15, 23	6, 9	9, 23	11	23
Maximum carrying capacity (MW)		12,000	12,000	12,000	13,000	11,000
Grid operation efficiency (%)		62	61	61	57	65
Construction cost (CNY billion)		86.2	88.1	88.7	101.4	81.2
Maintenance cost (CNY billion)		6.31	6.57	6.60	8.15	5.45
Load-shedding penalty cost (CNY billion)		1.365	1.461	1.422	0.945	1.666
Carbon trading cost (CNY billion)		0.041	0.042	0.042	0.041	0.043
Number of occurrences of commutation failure		3	4	4	3	4
Number of voltage crossings		0	0	0	0	0
Number of DC blocking occurrences		1	1	1	1	2
Frequency crossings		0	0	0	0	0

The results from the five evaluated schemes are detailed in Table 3, focusing on the number of DC line feeds, drop locations, rated capacity, and total operating costs. The highest DC capacity feed-in of 13,000 MW is provided by Scheme 4, but the lowest economic efficiency is incurred, costing CNY 1162 million more than scheme 1. Conversely, the smallest DC capacity feed-in of only 11,000 MW is associated with Scheme 5. Only the safety test constraints for N-1 faults are considered in this scheme, which, therefore, does not meet the peaking requirements, frequency stability, or dynamic voltage support capability of the AC system after a DC fault. A high frequency of commutation failure and DC blocking is also reported. DC feed-in of 12,000 MW is observed in Schemes 1, 2, and 3, each with varying DC drop locations. The lowest total cost of CNY 15,576.3 million and

the most efficient grid operation are achieved by Scheme 1. Potential DC phase change failures cannot be handled by Scheme 2 because of a three-phase short circuit fault on the AC line near the DC drop-off point, while Scheme 3 does not meet the peak demand of the system. Additionally, the lowest load-shedding penalty cost among the three, at CNY 136.5 million, is recorded for scheme 1, indicating more efficient operation and higher power supply reliability.

5.2.2. Stage 2: Installation Location and Capacity Modification Results

Next, we entered the required parameters for the second-stage model and addressed the multi-objective problem with varying scales using the deviation satisfaction method. The comparison results of the first- and second-stage optimization are shown in Table 4.

From the comparison in Table 3, it is evident that the primary objective of the first stage is to maximize the carrying capacity of the UHV DC feeder at the receiving end of the grid. The optimal solution achieved a carrying capacity of 12,000 MW at the receiving end, while the UHV DC line at drop point 15 was subsequently downgraded (from ± 800 kV to ± 500 kV) following the second stage of dynamic safety calibration. This adjustment was made in alignment with the goals of economic investment and utilization efficiency. The total savings in construction and maintenance costs after the modification amounted to CNY 5.14 billion, resulting in a 9% improvement in network efficiency. Despite incurring a higher load-cutting penalty of CNY 0.078 billion, the overall construction became more economical and practical. The final construction outcomes are illustrated in Figure 6.

The results above indicate that (1) the primary factors limiting the DC carrying capacity of the AC system are peak shifting capacity and voltage support capacity and (2) the effective short-circuit ratio index for UHV DC proposed in this paper effectively reveals the impact of dynamic voltage support capacity on the selection of the DC drop point.

5.2.3. Stage 2: Installation Location and Capacity Modification Results

In order to assess the effectiveness of the assessment model for the carrying capacity of the two-stage UHV DC construction proposed in this study, three scenarios for comparison were established. The comparison results under different fault constraints are presented in Table 5.

Table 4. The optimization results of the typical day stage 1 and stage 2 comparison.

Evaluation Indicators		Comparison of Capacity Results for UHV DC Construction	
		Optimal Scheme of Stage 1	Optimal Scheme of Stage 2
± 500 kV	Quantity	2	3
	Drop point	9, 17	9, 15, 17
± 800 kV	Quantity	2	1
	Drop point	15, 23	23
Maximum carrying capacity (MW)		12,000	10,000
Grid operation efficiency (%)		62	71
Construction cost (CNY billion)		86.2	81.5
Maintenance cost (CNY billion)		6.31	5.87
Load-shedding penalty cost (CNY billion)		1.365	1.287
Carbon trading cost (CNY billion)		0.041	0.032
Number of occurrences of commutation failure		3	3
Number of voltage crossings		0	0
Number of DC blocking occurrences		1	1
Frequency crossings		0	0

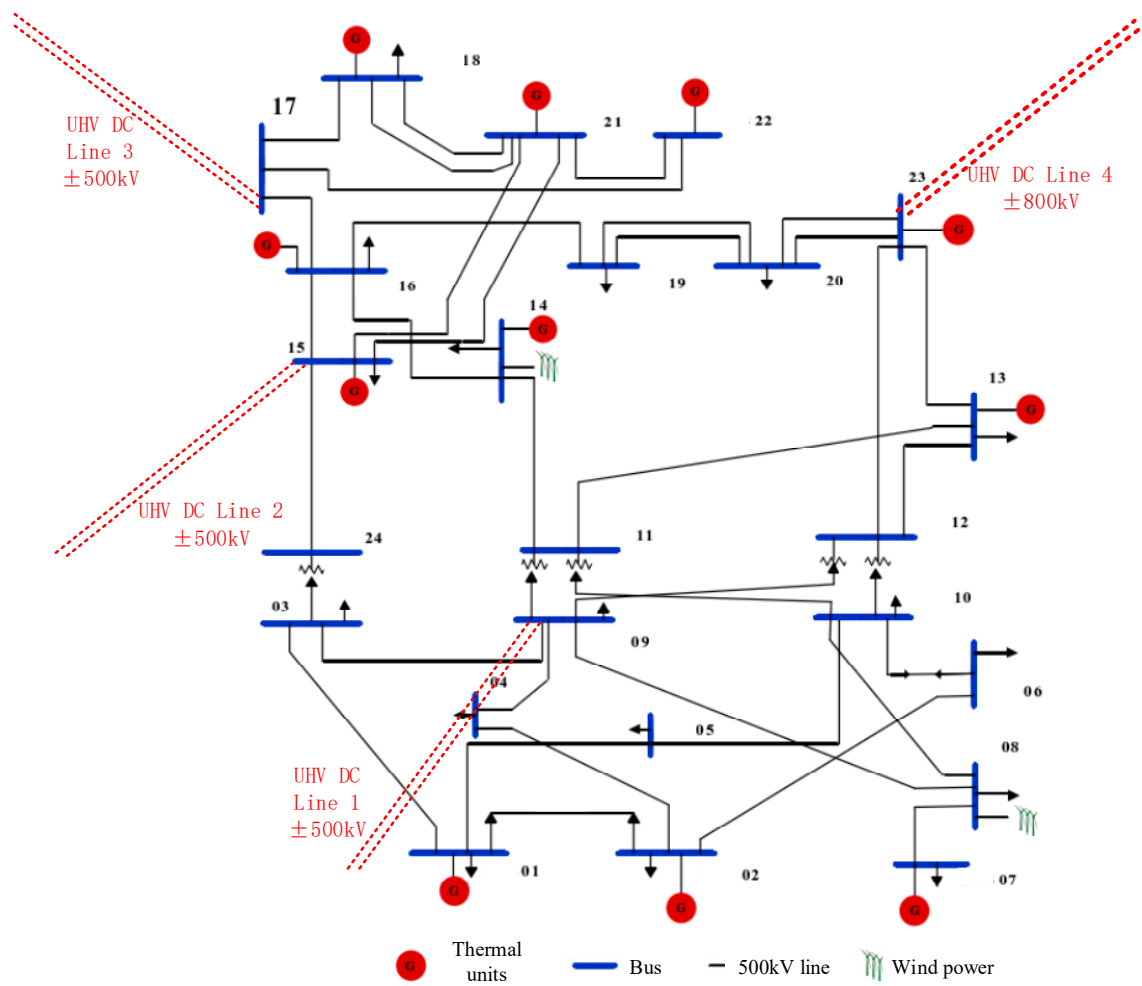


Figure 6. The final UHV DC construction outcomes in China.

Table 5. The comparison results under different fault constraints.

Evaluation Indicators		Comparison of Locating and Capacity Results for UHV DC Construction		
		Scenario 1	Scenario 2	Scenario 3
±500 kV	Quantity	2	3	3
	Drop point	6, 15, 17	6, 23	9, 15, 17
±800 kV	Quantity	2	1	1
	Drop point	23	17, 15	23
Maximum carrying capacity (MW)		10,000	12,000	10,000
Grid operation efficiency (%)		70	69	71
Construction cost (CNY billion)		82.3	86.6	81.5
Maintenance cost (CNY billion)		6.07	6.96	5.87
Load-shedding penalty cost (CNY billion)		2.478	1.478	1.287
Carbon trading cost (CNY billion)		0.031	0.033	0.032
Number of occurrences of commutation failure		5	4	3
Effective short circuit ratio of UHV DC line		3.1	3.5	3.7
Number of voltage crossings		1	1	0
Maximum frequency change rate (%)		0.92	0.66	0.51
Maximum frequency change (Hz)		0.13	0.07	0.04
Number of DC blocking occurrences		2	2	1
Frequency crossings		1	0	0

Scenario 1: Only N – 1 faults are considered (DC commutation failure, DC blocking, etc., are not taken into account).

Scenario 2: Multiple types of faults are considered, but only steady-state safety constraints are considered, without taking into account transient voltage support constraints in the event of commutation failure and frequency support constraints in the event of DC blocking.

Scenario 3: The carrying capacity assessment model for the two-stage UHV DC construction proposed in this study (based on scenario 2, taking into account transient voltage support constraints in the event of commutation failure and frequency support constraints in the event of DC blocking).

In Scenario 1, the maximum carrying capacity is higher than in Scenarios 2 and 3. However, it only considers safety test constraints for N-1 faults without evaluating all possible fault scenarios. Consequently, this scheme fails to meet frequency stability and dynamic voltage support requirements after DC faults. As illustrated in Figure 7, when a three-phase short-circuit occurs in the 8–9 node line, the effective short-circuit ratio of the Scenario 1 UHV DC line is lower than the voltage threshold. Additionally, Scenario 1 load-shedding cost (CNY 2.478 billion) is significantly higher than that of Scenario 2 and Scenario 3, indicating non-compliance with safety and stability standards. Scenario 2 does not account for transient voltage support under commutation failure conditions or frequency support under DC blocking conditions. Its MOESCR of 3.5 is lower than 3.7 in Scenario 3. This difference is because after a three-phase short-circuit fault in the AC line of Node 6-10 near DC Drop 6, the DC system in Scenario 2 has a higher probability of commutation failure and is more likely to experience voltage crossing and DC blocking. As shown in Figure 8, Scenario 2 fails to restore voltage promptly during the transient phase, leading to DC commutation failure. Ultimately, as depicted in Figure 9, Scenario 2 results in frequency deviation during the transient phase.

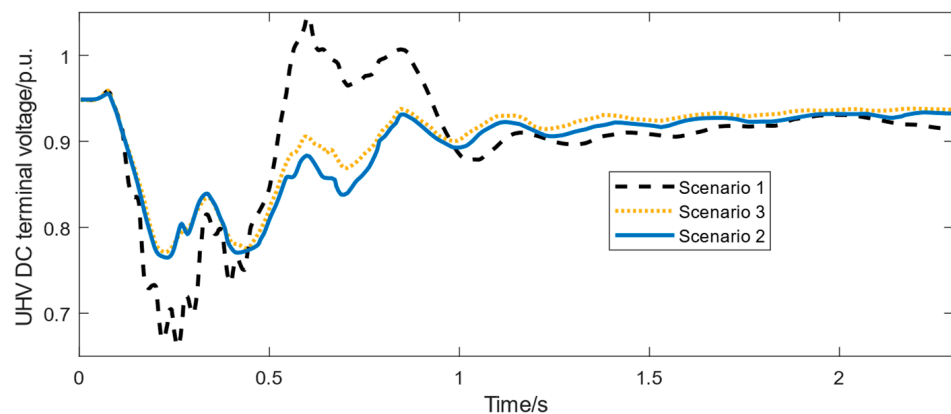


Figure 7. UHV DC terminal voltage at the three-phase short circuit of nodes 8 and 9.

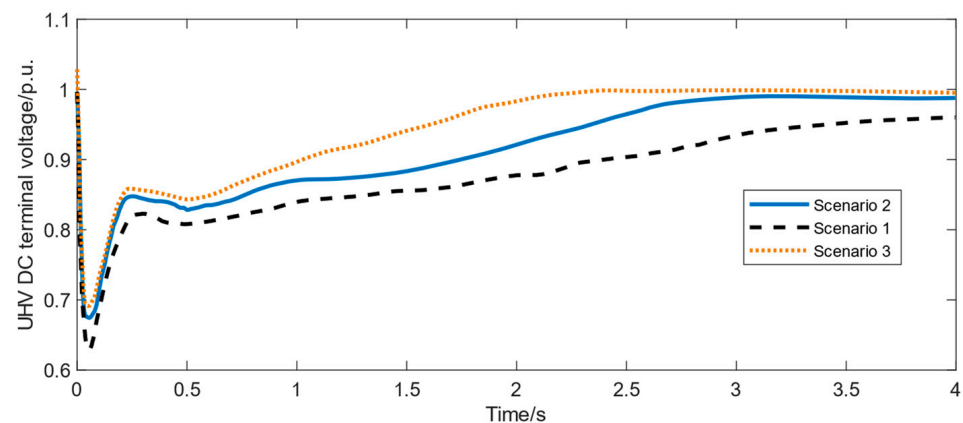


Figure 8. UHV DC terminal voltage at the three-phase short circuit of nodes 6 and 10.

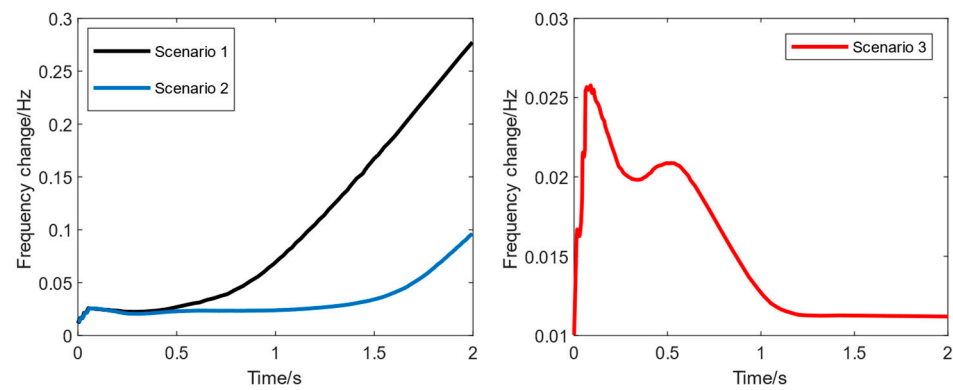


Figure 9. DC bipolar blocking frequency crossing results at the three-phase short circuit of nodes 6 and 10.

5.3. Parameter Sensitivity Analysis

5.3.1. Impact Analysis of CET Costs on Capacity Optimization of UHV DC

The implementation of carbon emissions trading policies can effectively control carbon emissions and reduce environmental pollution. This section analyzes the sensitivity of the carbon emissions trading price λ to carbon emissions and carbon emissions trading costs, as illustrated in Figure 10.

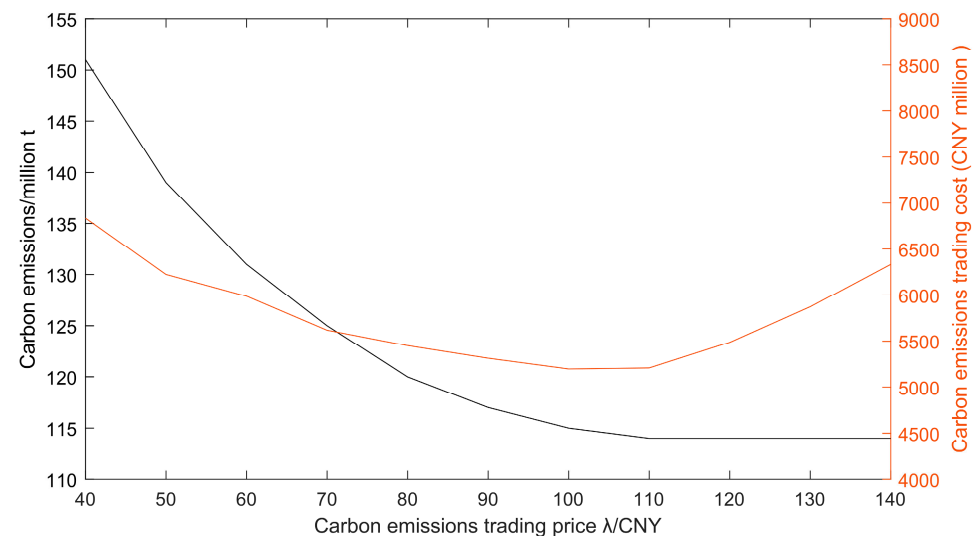


Figure 10. The relationship between carbon emissions trading price λ , carbon emissions.

It can be observed that as the carbon emissions trading price λ increases, the carbon emissions from thermal power units decrease, considering the cost-effectiveness of power generation. However, the carbon emissions trading cost comprises both carbon emissions and the trading price. When the trading price continues to rise despite the reduction in carbon emissions, the trading cost will also show an upward trend. Additionally, when the carbon emissions trading price λ is below CNY 110/t, the carbon emissions change significantly, and the trading cost shows a downward trend. When the trading price exceeds CNY 110/t, carbon emissions become insensitive to further price changes, and the trading cost rises significantly. Therefore, the carbon emissions trading mechanism can be applied flexibly, using the trading price λ as a lever to balance economic efficiency and low-carbon environmental protection, thereby sustaining the operation of a low-carbon economy.

5.3.2. Impact Analysis of Standby Capacity Confidence Level on Capacity Optimization of UHV DC

Firstly, it is essential to analyze the effect of the standby capacity confidence level ε on the system's standby capacity. Figure 11 illustrates the relationship between the confidence level ε and the system's standby capacity for each time period, assuming the confidence levels are set at 90%, 95%, and 99%, respectively.

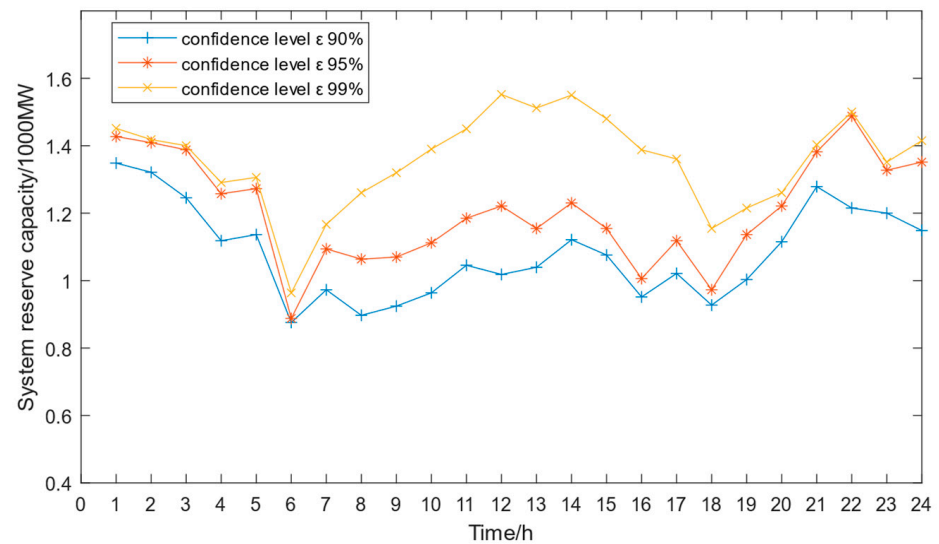


Figure 11. The relationship between confidence level ε and system reserve capacity.

It is observed that the peak reserve capacity occurs in the early morning hours when the confidence level ε is set at 90%, as most loads are supplied by thermal power units during this time. These units maintain a higher level of reserve capacity to prevent power supply shortages. When the confidence level ε is set at 99%, the highest reliability is required to prevent a sudden drop in PV output due to unexpected weather changes. Consequently, a higher level of reserve capacity is maintained at the peak of PV power generation. To further explore the relationship between confidence level and total system cost, Figure 12 depicts the relationship between confidence level and total system cost.

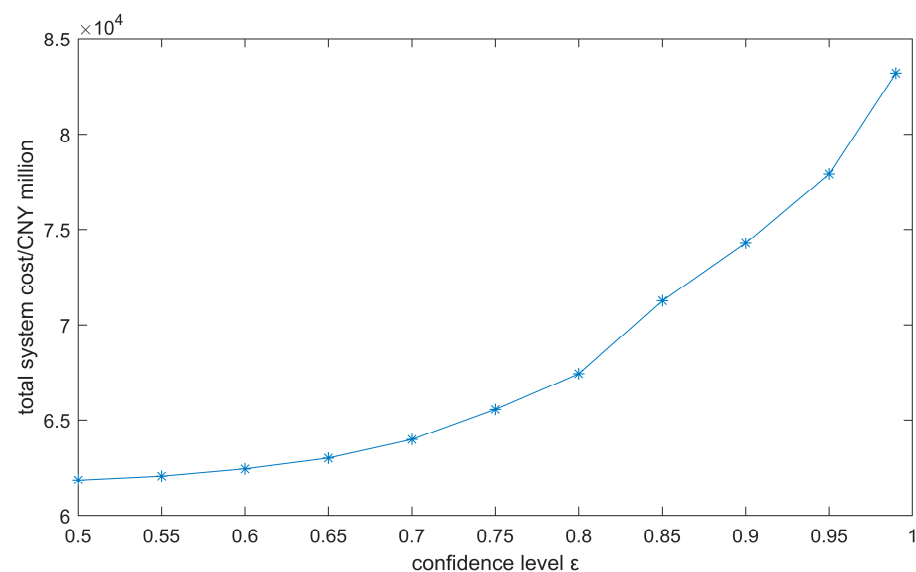


Figure 12. The relationship between confidence level ε and total system cost.

As the confidence level increases, the total system cost exhibits a monotonically increasing trend, with the growth rate accelerating. This phenomenon occurs because, as the confidence level rises, the system requires sufficient standby capacity to enhance its reliability, significantly increasing system costs. Therefore, by setting an appropriate probability constraint confidence level, a balance between the reliability and economy of the UHV DC channel can be achieved.

6. Conclusions and Future Work

6.1. Conclusions

The proposed UHV DC locating and capacity optimization model is validated for receiving grid in western China. The results show that the optimal configuration scheme maximizes the system economy, effectively suppresses the occurrence of DC commutation failure and DC blocking situations, and significantly enhances the dynamic frequency support strength of the system. The following conclusions can be drawn from the analysis of the results:

1. The proposed two-stage DC carrying capacity assessment model for the recipient end of the grid is capable of determining the optimal DC drop point and maximum DC carrying capacity while maintaining system peaking margin and disturbance immunity based on system size and intensity. The model achieves a maximum frequency deviation of 0.04 Hz in the AC network, an effective short circuit ratio of 3.7, and a load-shedding loss cost of CNY 128.7 million for all optimized levels. With a minimum investment scale of CNY 15.5637 billion to construct four UHV DC lines, the model satisfies UHV DC relative inertia constraints, peak shifting margin constraints, transient voltage support constraints during commutation fault conditions, and frequency support constraints during the DC blocking state.
2. Compared with evaluation models that only consider individual constraints such as N-1 safety checks, voltage support capability, and peak shifting capability, the model proposed in this paper achieves a smaller DC feeder size of 10,000 MW. However, the system demonstrates a stronger ability to withstand the risks of DC faults and has a sufficient peak shifting margin. The number of phase change failures (5 times) and DC blocking incidents (4 times) in the other schemes exceeds those in the proposed scheme (3 times). Additionally, their effective short-circuit ratios are lower than that of the proposed scheme (3.7), which fails to meet the requirements for peak margin and resistance to DC fault risks.
3. The discrepancy between the actual and predicted values of the equivalent load is offset by utilizing the surplus capacity, which is probabilistically constrained. In comparison with the conventional deterministic constraint, an appropriate confidence level for the probabilistic constraint can be established to achieve a balance between the reliability and cost-effectiveness of the UHV DC channel. Furthermore, the sensitivity analysis of the three-stage stepped carbon trading cost model reveals a significant variation in carbon emissions with changes in the carbon trading price λ ranging from 0 to 110 CNY/t. This can serve as a factor for optimizing the trade-off between system economics and low-carbon environmental preservation to sustain the operation of the system in a low-carbon and economically viable manner.

6.2. Limitations and Future Work

Currently, the planning of the Chinese UHV DC feeder grid is still undergoing continuous development and improvement. However, the existing strategies have certain limitations, and future research can focus on the following aspects:

1. Future optimization models for UHV DC planning can consider integrating novel energy storage systems [30] and user-side behaviors [31] to enhance their applicability in various scenarios.
2. With the strategic objective of achieving 'carbon peak, carbon neutral', China will phase out low-efficiency and high-energy consumption generators while increasing

the proportion of new energy output. Therefore, it is worth exploring a multi-stage DC carrying capacity assessment method for the receiving end grid in light of the gradual phasing out of conventional power sources and the construction timeline of UHV DC projects.

3. We will supplement the lack of research on the voltage or frequency stability problems involved in UHVDC with a large number of simulation studies in our future research.

Author Contributions: L.Z. conceptualized the idea of this research and carried out the theoretical analysis. Z.W. and Y.L. contributed to the design of the methodology and case study and writing and revising this paper. Y.W. provided important comments on the structure and format of this paper. T.Z. and H.Y. provided important comments on the language and the data for the example. H.S. contributed to the writing and revising of this paper. All authors have read and agreed to the published version of the manuscript.

Funding: This work was supported by the State Grid Science and Technology Project (No. 5100-202356023A-1-1-ZN).

Data Availability Statement: The original contributions presented in this study are included in this article. Further inquiries can be directed to the corresponding author.

Conflicts of Interest: Lang Zhao, Zhidong Wang, Yizheng Li and Tianqi Zhang were employed by the company State Grid Economic and Technological Research Institute Co., Ltd. Yao Wang was employed by Economic and Technological Research Institute of State Grid Shanxi Electric Power Co., Ltd. Haifeng Yu was employed by Economic and Technological Research Institute of State Grid Hunan Electric Power Co., Ltd. The authors declare that this research was conducted in the absence of any commercial or financial relationships that could be construed as a potential conflict of interest.

Nomenclature

W_t	standard Brownian motion
θ	a non-negative coefficient
$v(X_t)$	a non-negative function, which is defined on (l, u)
$\Gamma(x)$ and $\Gamma(x, a)$	the complete and incomplete gamma functions, respectively
v_{WT}^t	the simulated wind speed of the turbine at moment t
P_{WT}	the active power generated by the wind turbine
$P_{WT,r}$	the rated power of the wind turbine
v_{ci} and v_{co}	the cut-in and cut-out wind speeds
P_{stc}	the rated power labeled on the nameplate of the solar panel
T_t	the air temperature at moment t
α_T	the power temperature coefficient of the PV panels
T_{stc} and I_{stc}	the standard operating temperature and solar radiation intensity labeled on the nameplate
R_t	the irradiation intensity ratio between the tilted surface of the solar panel and the ground plane
I_{0t}	the solar irradiation outside the atmosphere
k_t	the clear-sky index
β	the ground inclination angle
ρ	the reflectivity of the ground
p and q	parameters related to the atmosphere
k_{th}	the maximum value of the clear-sky index
P_L	the actual active power of the load
μ_L and σ_L	the mean and standard deviation representing the load fluctuation
P_{EL}	equivalent load
E_q	the daily carbon emission quota
$M, N,$ and W	the number of thermal units, photovoltaic power generation units, and wind power generating units
$P_{MT,mt}, P_{PV,mt},$ and $P_{WT, \omega}$	the power generation per unit of thermal generation, photovoltaic power generation, and wind turbine generating units
E_p	the total daily carbon emission

H_m	the carbon emission per unit of power generated by the m -th traditional thermal units
f_e	the daily carbon emission cost
λ	the trading price per unit of carbon emission
$\max f_A$	the maximum capacity of the receiving end grid that can accommodate the UHV DC feed-in
Ω_h	the candidate set of pre-installed UHV DC lines
Ph_i^R	the rated capacity of the i -th UHV DC line
$\alpha_i, \beta_i,$ and γ_i	0–1 integer variables utilized to determine the construction specification of the i -th UHV DC line
$R_{MTm,t}$ and $R_{ESS,t}$	the standby capacity of the thermal power unit and energy storage system at time t
ε	the confidence level constant for this probabilistic constraint form
$p(i_{p,t}), w(i_{w,t}),$ and $l(i_{l,t})$.	the corresponding probability sequences
$N_{p,t}, N_{w,t},$ and $N_{l,t}$	the lengths of the probability sequences
$Pw_j^{max}, Pz_k^{max},$ and Pg_m^{max}	the maximum technical output of wind turbine j , photovoltaic power station k , and thermal power unit m
$\Omega_w, \Omega_s,$ and Ω_g	the collection of wind turbines, photovoltaic power stations, and
P_{lmax}	the maximum load of the receiving-end grid
GI and RI	the generating and load sufficiency coefficients
H_g	the inertia time constant of thermal power unit m
J_{AC}	the total inertia of the AC system
H_{UHV} and H_{DCmin}	the equivalent inertia time constant and the minimum equivalent inertia time constant of UHV DC
$Rh_{s,t,i}^{up}$ and $Rh_{s,t,i}^{down}$	the upper and lower standby capacities of UHV DC line i at moment t
d_t	the load-shedding penalty factor at moment t
$Pd_{s,t,d}$	the amount of load-shedding in the event of a DC fault d at moment t
$C_{v,i}$ and $C_{m,i}$	the construction cost and maintenance cost per unit length
$Pw_{s,t,j}, Pz_{s,t,k},$ and $Pg_{s,t,m}$	the outputs of wind turbine j , photovoltaic power plant k , and thermal power generator m in scenario s at moment t
δ_1 and δ_2	the deviation satisfaction weight values
f_{B1}^* and f_{B2}^*	the optimal values of the objective function under single objective
$Pw_j^{min}, Pz_k^{min},$ and Pg_m^{min}	the minimum technical outputs of wind turbine j , photovoltaic power plant k , and thermal power unit m
$Ph_{s,t,i}$	the transmission power of UHV DC line i at moment t in scenario s
Ph_i^{min}	the minimum transmission power of UHV DC line i
Rh_i^{up} and Rh_i^{down}	the maximum glide and climb power specified for UHV DC line i
$I_{s,t,i}^{up}$ and $I_{s,t,i}^{down}$	0–1 variables indicating whether the upward and downward power of the UHV DC line i at moment t in scenario s
$U_{s,t,i}$	a 0–1 variable indicating whether or not the adjustment is performed for moment t in scenario s for UHV DC line i
$T_{i,min}$	the minimum time for constant power operation of UHV DC line i
PCP^{min}, TCP^{min}	the minimum high and low peak capacity margins required for safe and stable operation
$MOESCR_i$	the effective short-circuit ratio of the i -th UHV DC line
$MOESCR_{min}$	the threshold value of the effective short-circuit ratio of the UHV DC line
η_{iq}	a 0–1 variable indicating whether the reactive power support equipment at node q has an effect on voltage restoration for DC line i
Q_{iq}	the reactive power provided by the reactive support equipment at node q to DC line i
Z_{iq} and Z_{qq}	the impedance and self-impedance of node q
$\Delta Pd_{s,t,i}^k$	the load-shedding amount for DC blocking fault k at moment t in scenario s
ΔPd^{max}	the maximum permissible load-shedding amount
Ω_{ds}	the set of nodes with automatic load-shedding devices
$\Delta P_{s,t}^k$	the unbalanced power generated by DC blocking faults at moment t in scenario s

$RoCOF_{max}$	the maximum rate of change in the frequency of the system. f_0
Δf_{max}	represents the rated frequency
$P_{EL,t}$	the maximum frequency deviation of the system
$f_{PV}(), f_{WT}(),$ and $f_L()$	the equivalent load at time t
$e(i_e)$	the probability density functions of PV, wind, and load, respectively
$\psi_{ie,t}$	the equivalent load P_{EL} probability density sequence
	$\psi_{ie,t}$ equals 1 when the standby capacity of the UHV DC channel is greater than or equal to the difference between $i_{e,t}q$ and $E(P_{EL,t})$;
	otherwise, $\psi_{ie,t}$ equals 0

References

- Chen, G.; Dong, Y.; Liang, Z. Analysis and reflection on high-quality development of new energy with Chinese characteristics in energy transition. *Proc. CSEE* **2020**, *40*, 5493–5505. (In Chinese)
- Zhang, X.; Liu, F.; Wang, S.; Li, Y. Measures to enhance new energy consumption in extra-high voltage direct current feeder grids. *Proc. CSU-EPSA* **2022**, *34*, 135–141.
- Tang, G.; Pang, H.; He, Z. Development and application of advanced AC/DC power transmission technology in China. *Proc. CSEE* **2016**, *36*, 1760–1771. (In Chinese)
- Liu, L.; Li, W.; Ba, Y. An analytical model for frequency nadir prediction following a major disturbance. *IEEE Trans. Power Syst.* **2020**, *35*, 2527–2536. [[CrossRef](#)]
- Mazzanti, G.; Diban, B. The Effects of Transient Over-voltages on the Reliability of HVDC Extruded Cables. Part 1: Long Temporary Overvoltages. *IEEE Trans. Power Syst.* **2021**, *36*, 3784–3794. [[CrossRef](#)]
- Hadavi, S.; Saunderson, J.; Mehrizi-Sani, A.; Bahrani, B. A Planning Method for Synchronous Condensers in Weak Grids Using Semi-definite Optimization. *IEEE Trans. Power Syst.* **2023**, *38*, 1632–1641. [[CrossRef](#)]
- Huang, H. A multi-scenario robust optimal scheduling method of distribution network considering source-side and load-side uncertainty based on the probability-box. *Power Supply Consum.* **2020**, *37*, 48–55.
- Zhu, Y.; Zhou, R.; Luo, L. Economic scheduling of power systems considering demand response and PV Uncertainty. *J. Sol. Energy* **2023**, *44*, 62–68.
- Qiu, G.; Zhang, P.; He, P. Robust economic optimal scheduling of power system considering wind power access. *Electr. Power Constr.* **2019**, *42*, 101–109.
- Yu, D.; Yang, P.; Tang, R.; Wang, Q.; Wang, C. Optimal scheduling method of regional integrated energy system based on stochastic differential equation. *Power Supply Electr.* **2022**, *39*, 89–95.
- Chen, X.; Lin, J.; Liu, F.; Song, Y. ITO Stochastic process model for new energy power generation. *Proc. CSEE* **2020**, *40*, 83–95+376.
- Yang, D.; Tu, Z.; Xu, J.; Ding, J.; Yang, J.; Xiao, Y. Two-layer planning of active distribution network with low carbon emission and demand side management. *J. Wuhan Univ. Eng. Sci.* **2022**, *55*, 709–715.
- Tian, B.; Chang, X.; Zhang, X.; Tian, K.; Wang, Z. Low-carbon economic dispatching of distribution network considering demand response and shared energy storage. *Electr. Power Demand Side Manag.* **2021**, *23*, 52–56.
- Meng, L.; Zhuo, C.; Yang, X.; Zhao, Z. Economic Optimal scheduling strategy for active distribution network considering light-load uncertainty and rotation reserve constraint. *Electr. Power Constr.* **2022**, *43*, 63–72.
- Zhang, N.; Hu, Z.; Dai, D.; Dang, S.; Yao, M.; Zhou, Y. Unit commitment model in smart grid environment considering carbon emissions trading. *IEEE Trans. Smart Grid* **2016**, *7*, 420–427. [[CrossRef](#)]
- Sheridan, L.M.; Phillips, C.; Orrell, A.C.; Berg, L.K.; Tinneland, H.; Rai, R.K.; Zisman, S.; Duplyakin, D.; Flaherty, J.E. Validation of wind resource and energy production simulations for small wind turbines in the United States. *Wind Energy* **2022**, *7*, 659–676. [[CrossRef](#)]
- Chen, Q.; Li, H.; Wang, S.; Shi, R.; Zhang, N.; Qi, Q.; Wang, F. Multi-energy complementary time-series simulation technology for promoting RE consumption. *China Electr. Power Constr.* **2019**, *40*, 18–25.
- Suo, Z.; Liu, J.; Jiang, W.; Li, Z.; Yang, L. Research on the configuration of regulator for large-scale new energy DC transmission system. *Electr. Power Autom. Equip.* **2019**, *39*, 124–129.
- Chang, N.; Huo, C.; Liu, F.; Ke, X.; Hou, Y.; Niu, S.; Wang, C. Research on optimal configuration of regulating camera for improving transient voltage stability level of weak feeder grid. *Power Syst. Prot. Control.* **2019**, *47*, 90–95.
- Yang, J.; Shi, Z.; He, C.; Li, X.; Liang, Y. Optimal configuration strategy of condenser for improving short-term voltage safety in a sending-end power grid with a high renewable penetration level. *J. Shandong Univ. Eng. Sci.* **2024**, *54*, 174–182.
- Wang, Q.; Li, T.; Tang, X.; Liu, F.; Lei, J. Method of site selection for synchronous condenser responding to commutation failures of multi-infeed DC system. *Autom. Electr. Power Syst.* **2019**, *43*, 222–227. (In Chinese)
- Zhou, Y.; Sun, H.; Xu, S.; Wang, X.; Zhao, B.; Zhu, Y. Synchronous condenser optimized configuration scheme for power grid voltage strength improvement. *Power Syst. Technol.* **2022**, *46*, 3848–3856. (In Chinese)
- Zhang, Z.; Zhou, M.; Wu, Z.; Liu, J.; Liu, S.; Guo, Z. An energy storage siting and capacity planning method considering dynamic frequency support. *Proc. CSEE* **2023**, *43*, 2708–2721.

24. Badawi, M.; Ibrahim, S.A.; Mansour, D.E.A.; Ward, S.A.; El-Faraskoury, A.A.; Ghali, M. On highlighting the merits of gas-to-liquid transformer oil under accelerated thermal aging and faults: Electrical and physio-chemical properties. *IEEE Access* **2024**, *12*, 93372–93388. [[CrossRef](#)]
25. El-Faraskoury, A.; Ward, S.A.; Mansour, D.E.A.; Ibrahim, S.A. Oil Condition Assessment for Aged Transformers Based on Dissolved Gas Analysis. In Proceedings of the 2023 24th International Middle East Power System Conference, MEPCON, Mansoura, Egypt, 19–21 December 2023; pp. 135–142.
26. Li, G.; Li, X.; Bian, J.; Niu, J.; Ding, H.; Chen, W. Multidimensional time series simulation of large-scale photovoltaic power plant output based on hourly clear sky index. *Power Grid Technol.* **2020**, *44*, 3254–3262.
27. Lin, F.; Zhang, Y.; Dong, Q.; Cui, G.; Wang, J.; Zhu, M. Probability prediction of photovoltaic output based on Quantile interpolation and deep autoregressive network. *Power Syst. Autom.* **2023**, *47*, 79–87.
28. Zhang, Y.; Xu, Y.; Zhang, R.; Dong, Z.Y. A missing-data tolerant method for data-driven short-term voltage stability assessment of power systems. *IEEE Trans. Smart Grid* **2019**, *10*, 5663–5674. [[CrossRef](#)]
29. Chen, P.; Guan, L. Research on analysis and modelling of dynamic reactive power demand and its power recovery characteristics in DC transmission system. *Mod. Electr. Power* **2017**, *34*, 50–58.
30. Huang, W.; Zhang, B.; Ge, L.; He, J.; Liao, W.; Ma, P. Day-ahead optimal scheduling strategy for electrolytic water to hydrogen production in zero-carbon parks type microgrid for optimal utilization of electrolyzer. *Energy Storage* **2023**, *68*, 107653. [[CrossRef](#)]
31. Giannelos, S.; Borozan, S.; Aunedi, M.; Zhang, X.; Ameli, H.; Pudjianto, D.; Konstantelos, I.; Strbac, G. Modelling Smart Grid Technologies in Optimisation Problems for Electricity Grids. *Energies* **2023**, *16*, 5088. [[CrossRef](#)]

Disclaimer/Publisher’s Note: The statements, opinions and data contained in all publications are solely those of the individual author(s) and contributor(s) and not of MDPI and/or the editor(s). MDPI and/or the editor(s) disclaim responsibility for any injury to people or property resulting from any ideas, methods, instructions or products referred to in the content.